



HAL
open science

The gammaproteobacterium *Achromatium* forms intracellular amorphous calcium carbonate and not (crystalline) calcite

Karim Benzerara, Romain Bolzoni, Caroline Monteil, Olivier Beyssac, Olivier Forni, Béatrice Alonso, Maria Asta, Christopher T. Lefèvre

► To cite this version:

Karim Benzerara, Romain Bolzoni, Caroline Monteil, Olivier Beyssac, Olivier Forni, et al.. The gammaproteobacterium *Achromatium* forms intracellular amorphous calcium carbonate and not (crystalline) calcite. *Geobiology*, 2021, 19 (2), pp.199-213. 10.1111/gbi.12424 . hal-03086061

HAL Id: hal-03086061

<https://cnrs.hal.science/hal-03086061>

Submitted on 22 Dec 2020

HAL is a multi-disciplinary open access archive for the deposit and dissemination of scientific research documents, whether they are published or not. The documents may come from teaching and research institutions in France or abroad, or from public or private research centers.

L'archive ouverte pluridisciplinaire **HAL**, est destinée au dépôt et à la diffusion de documents scientifiques de niveau recherche, publiés ou non, émanant des établissements d'enseignement et de recherche français ou étrangers, des laboratoires publics ou privés.

1 **The gamaproteobacterium *Achromatium* forms intracellular amorphous calcium**
2 **carbonate and not (crystalline) calcite**

3
4 Running title: *Achromatium* forms ACC and not calcite

5
6 Benzerara Karim^{1*}, Bolzoni Romain², Monteil Caroline², Beyssac Olivier¹, Forni Olivier³,
7 Alonso Béatrice², Asta Maria P.⁴, Lefevre Christopher²

8
9 ¹Sorbonne Université, Muséum National d'Histoire Naturelle, UMR CNRS 7590. Institut de
10 Minéralogie, de Physique des Matériaux et de Cosmochimie (IMPMC), 4 Place Jussieu, 75005
11 Paris, France.

12 ²Aix-Marseille University, CNRS, CEA, UMR7265 Institute of Biosciences and Biotechnologies
13 of Aix-Marseille, CEA Cadarache, F-13108 Saint-Paul-lez-Durance, France

14 ³Institut de Recherche en Astrophysique et Planétologie (CNRS, Univ. Toulouse, CNES),
15 Toulouse, France

16 ⁴University Grenoble Alpes, CNRS, IRD, IFSTTAR, ISTERre, 38000, Grenoble, France

17
18 * Corresponding author

19 Tel.: +33(0)144277542

20 E-mail address: karim.benzerara@sorbonne-universite.fr

21
22 **Acknowledgements**

23 This project has received funding from the CNRS: “Programme national Ecosphère
24 Continentale et Côtière (EC2CO)” (BACCARAT2 – N°13068), the French National Research
25 Agency (SIGMAG: ANR-18-CE31-0003 and PHOSTORE: ANR-19-CE01-0005-02), and the
26 European Union’s Horizon 2020 research and innovation programme under the Marie
27 Skłodowska-Curie grant agreement 747597. We thank Fériel Skouri-Panet and Cynthia Travert
28 for user support on the IMPMC Biology facility, and Imène Esteve, Béatrice Doisneau and
29 Stéphanie Delbrel for user support on the IMPMC SEM facility. We declare no conflict of
30 interest.

31

32 **Data Availability Statement**

33 The data that support the findings of this study are openly available in zenodo at
34 <http://doi.org/10.5281/zenodo.4295976> and in NCBI for DNA sequences.

35

36

37

38

39

40

41

42

43

44

45

46

47

48

49

50

51

52

53

54

55

56

57

58

59

60

61

62 **Abstract**

63 *Achromatium* is a long known uncultured giant gammaproteobacterium forming intracellular
64 CaCO_3 that impact C and S geochemical cycles functioning in some anoxic sediments and at
65 oxic-anoxic boundaries. While intracellular CaCO_3 granules have first been described as Ca
66 oxalate then colloidal CaCO_3 more than one century ago, they have often been referred to as
67 crystalline solids and more specifically calcite over the last 25 years. Such a crystallographic
68 distinction is important since the respective chemical reactivities of amorphous calcium
69 carbonate (ACC) and calcite, hence their potential physiological role and conditions of
70 formation, are significantly different. Here we analyzed the intracellular CaCO_3 granules of
71 *Achromatium* cells from Lake Pavin using a combination of Raman microspectroscopy and
72 scanning electron microscopy. Granules in intact *Achromatium* cells were unequivocally
73 composed of amorphous calcium carbonate (ACC). Moreover, ACC spontaneously
74 transformed into calcite when irradiated at high laser irradiance during Raman analyses. Few
75 ACC granules also transformed spontaneously into calcite in lysed cells upon cell death and/or
76 sample preparation. Overall, the present study supports the original claims that intracellular Ca-
77 carbonates in *Achromatium* are amorphous and not crystalline. In that sense, *Achromatium* is
78 similar to a diverse group of Cyanobacteria and a recently discovered magnetotactic
79 alphaproteobacterium, which all form intracellular ACC. The implications for the physiology
80 and ecology of *Achromatium* are discussed. Whether the mechanisms responsible for the
81 preservation of such unstable compounds in these bacteria are similar to those involved in
82 numerous ACC-forming eukaryotes remains to be discovered. Last, we recommend to future
83 studies addressing the crystallinity of CaCO_3 granules in *Achromatium* cells recovered from
84 diverse environments all over the world to take care of the potential pitfalls evidenced by the
85 present study.

86 **Keywords: Raman; intracellular biomineralization; micromanipulation; ACC**

87

88 1. Introduction

89 *Achromatium oxaliferum* has first been fully described by Schewiakoff (1893). Since then, it
90 has been shown that the genus *Achromatium* groups a diversity of giant colorless sulfur-
91 oxidizing bacterial species which form intracellular elemental S⁰ and CaCO₃ granules (Gray &
92 Head, 2014). They are widely distributed worldwide at the oxic-anoxic boundary in sediments
93 of freshwater, brackish and marine environments (Ionescu et al., 2020; Salman et al., 2015).
94 Since they can represent a relatively high biovolume, up to 90% of the total microbial volume
95 in a sediment, they have received particular attention. No strain has been cultivated so far but
96 culture-independent methods have been used to infer their physiology and ecology (e.g.,
97 Ionescu et al., 2017; Mansor et al., 2015). *Achromatium* cells have been reported to live in the
98 sulfate reduction zone, sometimes in areas of low free sulfide activity, at least for freshwater
99 representatives (Gray & Head, 2014). They oxidize sulfide to elemental sulfur using O₂ or
100 possibly nitrates (Salman et al., 2015). Some populations have been reported to be autotroph
101 for C while others might be organotroph (Gray et al., 1999). *Achromatium* cells may have a
102 significant role in local geochemical cycles of Ca since they form large amounts of intracellular
103 CaCO₃ granules. Moreover, they sometimes produce these granules in solutions undersaturated
104 with all Ca-carbonate mineral phases. In these sediments, *Achromatium* cells are the sole
105 carriers of Ca-carbonates (Gray & Head, 2014). Consistently, freshwater sediments from a
106 wetland region close to Rydal Water (UK) have been reported to show a correlation between
107 the solid-phase calcium content and *Achromatium* cell numbers (Head et al., 2000). Since the
108 dynamics of the cells is associated with the dynamics of the oxic-anoxic boundary, it creates a
109 unique connection between variations of redox conditions and carbonate formation.

110 The function of the intracellular CaCO₃ granules has been widely questioned. For example, it
111 has been suggested that these intracellular Ca-carbonate granules may buffer intracellular pH
112 variations associated with sulfur oxidation (e.g., Salman et al., 2015). This idea has been

113 supported by the recent observations that these Ca-carbonate granules dissolved when cells
114 were exposed to oxygen and sulfur oxidation was promoted (Yang et al., 2019). In contrast,
115 Schorn et al. (2020) suggested that the CaCO₃ granules are located in the periplasmic space of
116 *Achromatium* cells, therefore raising questions about this intracellular pH buffering function of
117 CaCO₃. An alternative, suggested and also debated, function for CaCO₃ granules is that they
118 may serve as ballasts in *Achromatium* and anchor cells to the sediment close to the oxic-anoxic
119 boundary (N. Gray & Head, 2014).

120 All members of the *Achromatium* genus form intracellular Ca-carbonates and it has long been
121 thought that this biomineralization process was specific to this bacterial taxon. However,
122 widespread and phylogenetically diverse cyanobacteria have been shown to be able to
123 biomineralize intracellular Ca-carbonates as well (Benzerara et al., 2014; Couradeau et al.,
124 2012). Li et al. (2016) showed that the intracellular Ca-carbonates are amorphous calcium
125 carbonates (ACC) in all these cyanobacteria. Moreover, a magnetotactic bacterium affiliated to
126 Alphaproteobacteria was recently shown to biomineralize intracellular ACC as well (Monteil
127 et al., 2020). Last, many eukaryotes have also been shown to biomineralize ACC instead of
128 crystalline calcite or aragonite, at least as a precursor phase (Addadi et al 2003). Whether this
129 capability to form intracellular CaCO₃ convergently appeared several times during evolution in
130 these organisms or it involves homologous pathways (in connection with e.g., C fixation)
131 remains to be determined by future molecular biology approaches.

132 There are discrepancies in the literature about the nature of the intracellular Ca-carbonates in
133 *Achromatium* (Table S1). These discrepancies started as early as *Achromatium* was discovered.
134 Indeed, Schewiakoff (1893) followed by, e.g., Virieux (1913) first suggested that intracellular
135 granules were composed of calcium oxalate. This interpretation was based on the observation
136 of recrystallized granules extracted from *Achromatium* cells by various reactants, which looked
137 like the Ca-oxalates formed by plants. However, a few years later, West and Griffiths (1913),

138 also using various chemical tests, concluded that the granules were calcium carbonates. At that
139 time, they thought that they were analyzing cells belonging to a genus different from the one
140 analyzed by Schewiakoff (1893), which they named *Hillhousia viirabilis*, but it was later shown
141 to be *Achromatium* as well. Moreover, West and Griffiths (1913) mentioned that the CaCO₃
142 granules in the cells did not polarize and only crystallized when extracted from the cells. They
143 therefore concluded that the calcium carbonate granules within the cells were in “a colloidal
144 form” and different from the ones in dead organisms. Bersa (1926) reiterated similar
145 experiments and again suggested that *Achromatium* granules were composed of amorphous
146 CaCO₃. However, we noticed that authors have started to mentioned calcite instead of
147 amorphous CaCO₃ at least since 1991 (e.g., Babenzien, 1991). Head et al. (1995) and Head et
148 al. (2000) directly addressed the question of the crystallinity of *Achromatium* CaCO₃ granules
149 by performing x -ray diffraction analyses of purified preparations of intact cells and suggested
150 that the granules were calcite and not another structural form. Interestingly, Gray (2006)
151 mentioned calcite but specified that this calcite may not be purely crystalline. More recently,
152 Salman et al. (2015) analyzed Ca-carbonate granules *in situ* within *Achromatium* cells by
153 Raman microspectroscopy and also concluded that they were calcite crystals. Consistently,
154 most recent studies assumed that intracellular granules were calcite crystals based on the latest
155 reports in the literature (e.g., Babenzien et al., 2015; Ionescu et al., 2017; Mansor et al., 2015;
156 Schorn & Cypionka, 2018; Yang et al., 2019). Yet, the observations by West and Griffiths
157 (1913) suggesting that *Achromatium* CaCO₃ granules are composed of ACC seem precisely
158 documented. Moreover, the presence of intracellular ACC in cyanobacteria and the recently
159 discovered magnetotactic alphaproteobacterium urges new efforts in characterizing the
160 crystallinity of CaCO₃ granules in *Achromatium*. If there was a difference between
161 *Achromatium* and other bacteria, this would suggest that specific mechanisms are involved in
162 *Achromatium* and other bacteria in order to crystallize Ca-carbonate or preserve ACC from

163 crystallization and they would need to be investigated in the future. Moreover, since ACC and
164 calcite have different thermodynamic properties, they may hold different functional roles and/or
165 the same role but with different efficiencies. Consequently, we re-investigated the nature of the
166 CaCO₃ granules in *Achromatium* cells by conducting Raman analyses on *Achromatium*
167 populations found in the sediments of Lake Pavin.

168

169 **2. Material & Methods**

170

171 **2.1 Site description and sample collection**

172 Sediments were collected on the shore of Lake Pavin, Massif Central, France in November
173 2019. Sampling was achieved by filling one-litre glass bottles with 300-400 mL of sediments
174 and 600-700 mL of water that overlaid the sediments. Air bubbles were excluded. Once in the
175 laboratory, bottles were stored with their cap closed, under dim light and at room temperature
176 (~25°C) from a few days up to a few months. The sampling location at Lake Pavin was
177 45.499107°N, 2.886273°E. No *in situ* measurement of O₂, sulfate and sulphide profiles was
178 conducted on these samples. However, a previous study showed that the oxic-anoxic boundary
179 extended in the first five millimetres of the sediments (Monteil et al., 2020).

180

181 **2.2 Light microscopy observations, cell sorting and whole genome amplification (WGA)**

182 Observation and micromanipulation were carried out on a 20-μL drop of pore water harvested
183 in the first millimetre below the interface water/sediments of a sample collected in Lake Pavin.
184 Cell sorting was done with an InjectMan® NI2 micromanipulator and a CellTram® vario,
185 hydraulic, manual microinjector from Eppendorf mounted on a Leica DM IL LED microscope
186 equipped with a 63x/0.70 PH objective. The microscope and micromanipulator were placed
187 inside a clean chamber exposed beforehand for 1 h to ultraviolet germicidal irradiation
188 (wavelength of the lamp: 254 nm). Single-cells with an ultrastructure and granules typical of

189 *Achromatium* species were transferred two consecutive times with a sterile microcapillary into
190 a 4- μ L drop of Lake Pavin water filtered at 0.2 μ m, before their final transfer into a 4- μ L drop
191 of phosphate buffer saline (PBS). This drop was stored at -20°C before WGA. To obtain
192 sufficient gDNA for 16S rRNA gene sequencing, WGA was carried out using the multiple
193 displacement amplification (MDA) technique with the REPLI-g Single-Cell Kit (QIAGEN)
194 following the manufacturer's instructions.

195

196 **2.3 Cloning and sequencing of the 16S rRNA genes**

197 The 16S rRNA gene was amplified using the Phusion[®] Hot Start Flex DNA Polymerase
198 following the manufacturer's recommendations, a DNA template of 50 - 70 ng/ μ l and the 27F
199 5'-AGAGTTTGATCMTGGCTCAG-3' and 1492R 5'-TACGGHTACCTTGTTACGACTT-
200 3' primers (Lane, 1991). Blunt-end fragments of 16S rRNA gene sequences were cloned using
201 a Zero Blunt[®] TOPO[®] PCR Cloning Kit with One Shot[®] TOP10 chemically competent *E. coli*
202 cells. The inserts were sent for sequencing (Eurofins Genomics Germany GmbH). Sequences
203 were compared to data found in the NCBI nucleotide database using the Basic Local Alignment
204 Search Tool. Sequences were deposited in the NCBI Genbank database under the accession
205 numbers MN990460 and MN990461.

206

207 **2.4 Phylogenetic analyses**

208 The 16S rRNA gene sequences of representative type strains of all Thiotrichales
209 (Gammaproteobacteria) families were downloaded from the public NCBI database (January
210 2020). This database was enriched with several sequences related to the *Achromatium* genus,
211 some of the newly described candidate Thiotrichales species and the sequences of the two Lake
212 Pavin CaCO₃-accumulating OTUs (Pavin-1 and Pavin-2). The 52 sequences were aligned using
213 MAFFT 7 (Kato & Standley, 2013) and trimmed using Gblocks (Talavera & Castresana, 2007)
214 to get a final alignment of 1410 bp. A maximum- likelihood (ML) tree was built with RAxML

215 8.2.6 (Stamatakis, 2014) under the GAMMAI model of rate heterogeneity and the GTR
216 substitution model. A total of 350 bootstrap replicates automatically determined by the MRE-
217 based bootstopping criterion were conducted using the rapid bootstrapping algorithm, among
218 which 100 were sampled to generate proportional support values. In this phylogeny, members
219 of the Francisellaceae and Fastidiosibacteraceae families were used to root the tree based on
220 previous phylogenies of the Thiotrichales order (Xiao et al., 2018).

221

222 **2.5 Preparation of cells for microscopy analyses**

223 Lake Pavin *Achromatium* cells were sorted by micromanipulation and directly deposited on a
224 glass coverslip (18 x 18 mm) coated with poly-L-lysine to improve cells' adhesion. Raman
225 microspectroscopy analyses were conducted first with a systematic localization of the analyzed
226 cells. The coverslip was then sputtered with carbon. Cells analyzed by Raman were relocated
227 and further analyzed by scanning electron microscopy (SEM). We note that the assessment of
228 CaCO₃ crystallinity was performed by Raman spectroscopy before C-sputtering and therefore
229 we presently do not know if the later step may induce ACC crystallization. Moreover, air-drying
230 of cells, exposition of cells to vacuum and C-sputtering can cause cell damages, in particular
231 flattening. However, in the present study only the features that were not affected (such as
232 presence/absence of a cell wall) were investigated.

233

234 **2.6 Reference ACC synthesis and thermogravimetric analyses**

235 ACC synthesis was carried out following the procedure described by Wang et al. (H.-W. Wang
236 et al., 2017). Fresh solutions of 100 ml of 50 mM CaCl₂ and 50 mM Na₂CO₃ (+ 0.5 g NaOH)
237 were prepared with cold (4°C) MilliQ water. The CaCl₂ solution was placed in a 500 mL Teflon
238 centrifuge bottle. A 30 x 30 cm², 75 mm thick polyethylene sheet was placed in the upper part
239 of the centrifuge bottle with a steel ball (1 cm in diameter, 5 g). The Na₂CO₃-NaOH solution
240 was poured into the polyethylene sheet, keeping both solutions separated. The bottle was then

241 placed in a centrifuge (Beckman Coulter model Avanti J-20 XP) pre-cooled to 4 °C, and it was
242 spun at 4000 rpm for 3 minutes. The force exerted by the ball on the polyethylene sheet breaks
243 the sheet and throws the Na₂CO₃–NaOH solution into the CaCl₂ solution extremely rapidly.
244 The supernatant liquid was poured out and the solid was rinsed with a few mL of dry cold (4°C)
245 acetone. The suspension in acetone was filtered on a Buechner funnel, the solid was recovered
246 and dried at room temperature under vacuum for 4-5 h.
247 Thermogravimetric analysis-differential scanning calorimetry (TGA-DSC) analyses of the
248 reference ACC were performed using a METTLER TOLEDO® TGA/DSC3+. 8.6 mg of dry
249 powdered sample were placed in an alumina crucible and the sample was heated from 25 to
250 750°C under a 20mL/min N₂ flow. The temperature scanning rate was set at 20°C per minute.
251 Noteworthy, TGA-DSC analyses could not be performed on natural samples due to limited
252 amounts of sample.

253

254 **2.7 Raman microspectroscopy analyses**

255 Raman spectra were recorded using a Renishaw InVia Reflex spectrometer equipped
256 with a 532 nm Renishaw diode laser. The laser was focused on the sample using a DM2500
257 Leica microscope with a 100× objective (NA= 0.75) to obtain a planar resolution of ~ 1 μm².
258 The maximum laser power was measured at ~90 mW under the microscope without the
259 objective. The laser incident beam was polarized circularly by a quarter wavelength plate placed
260 before the microscope. We selected several neutral density filters to acquire Raman spectra at
261 varying laser powers from 0.1 up to 100% of the maximum laser power. Therefore, at 1%, the
262 power delivered in a 1 μm² spot was 900 μW and the irradiance was 9.10⁸ W.m⁻². The signal
263 was filtered by edge filters and dispersed by a diffraction grating with 2400 grooves/mm and
264 the signal was analyzed with a RENCAM CCD (charge-coupled device) detector. Before each

265 session, the spectrometer was calibrated in energy using a silicon standard. Spectra were
266 collected using the software WIRE 4.3 provided by Renishaw.

267 It has been shown that Raman spectra of the different CaCO₃ crystalline polymorphs (calcite,
268 aragonite, vaterite) are significantly different from each other and can therefore be used as
269 unambiguous signatures of these phases (Behrens et al., 1995). The ν_1 Raman bands of ACC
270 and calcite were fitted with 2 Voigt functions using the FitViewer program, a Graphical User
271 Interface (GUI) designed by Olivier Forni and Paolo Pilleri at the Institut de Recherche en
272 Astrophysique et Planétologie (IRAP). The fit was performed with the MPFIT algorithm
273 (Markwardt, 2009) which is based on the Levenberg-Marquardt method (Moré, 1978). As
274 further described by (Váci, 2014), the profile described by the Voigt function results from the
275 convolution of a Lorentzian profile by a Gaussian function. A Gaussian profile was assumed to
276 model the instrumental contribution and its FWHM was fixed at 1.9 cm⁻¹, equal to the
277 spectrometer bandpass as measured experimentally using the emission band of a Ne lamp. In
278 turn, the Lorentzian function is assumed to model the Raman transitions, corrected from the
279 instrumental response.

280

281 **2.8 Scanning Electron Microscopy**

282 Scanning electron microscopy (SEM) analyses were performed using a Zeiss ultra 55 field
283 emission gun SEM. Secondary electron (SE2) images were acquired using an Everhart
284 Thornley detector at an accelerating voltage of 2.0 kV and a working distance of ~3.5 mm.
285 Backscattered electron images were acquired for chemical mapping using an angle selective
286 backscattered (AsB) detector at an accelerating voltage of 15 kV and a working distance of
287 ~7.5 mm. Elemental maps were generated from hyperspectral images (HyperMap) by energy
288 dispersive X-ray spectrometry (EDXS) using an EDS QUANTAX detector. EDXS data were
289 analyzed using the ESPRIT software package (Bruker).

290 **3. Results**

291

292 Some pore water harvested from the first millimetres below the water/sediment interface was
293 deposited on a glass slide and examined under the light microscope. Large cells were observed,
294 measuring on average $22.3 \pm 6.7 \mu\text{m}$ in length and $14.2 \pm 4.0 \mu\text{m}$ in width (31 measurements),
295 which corresponded to volumes between ~ 500 and $3000 \mu\text{m}^3$ (Figure 1). They contained
296 numerous intracellular inclusions measuring around $3 \pm 1.3 \mu\text{m}$ in diameter (18 measurements,
297 4 cells). Five cells were sorted and the 16S rRNA gene of two of them was successfully
298 sequenced after whole genome amplification. Their 16S rRNA gene sequences clustered in the
299 *Achromatium* cluster A (Figure 2) as defined by Mansor et al. (2015). They shared 96 to 97%
300 sequence identity with the *Achromatium* L79966 and AF129550 OTUs, sequenced from a
301 wetland on the margins of Rydal Water and an upland tam on Jenny Dam, respectively, both
302 located in the United Kingdom and composed of freshwater as in Lake Pavin (Gray et al., 1999).
303 Moreover, *Achromatium* cells in Lake Pavin had a size range consistent with that of
304 *Achromatium* cells previously observed in Rydal water (cell volumes between 1000 and 30,000
305 μm^3) and the Jenny Dam (cell volumes between 150 and 26,000 μm^3).

306

307

308

309

310

311



312 **Figure 1:** Light microscopy images of *Achromatium* cells isolated from Lake Pavin sediments.

313

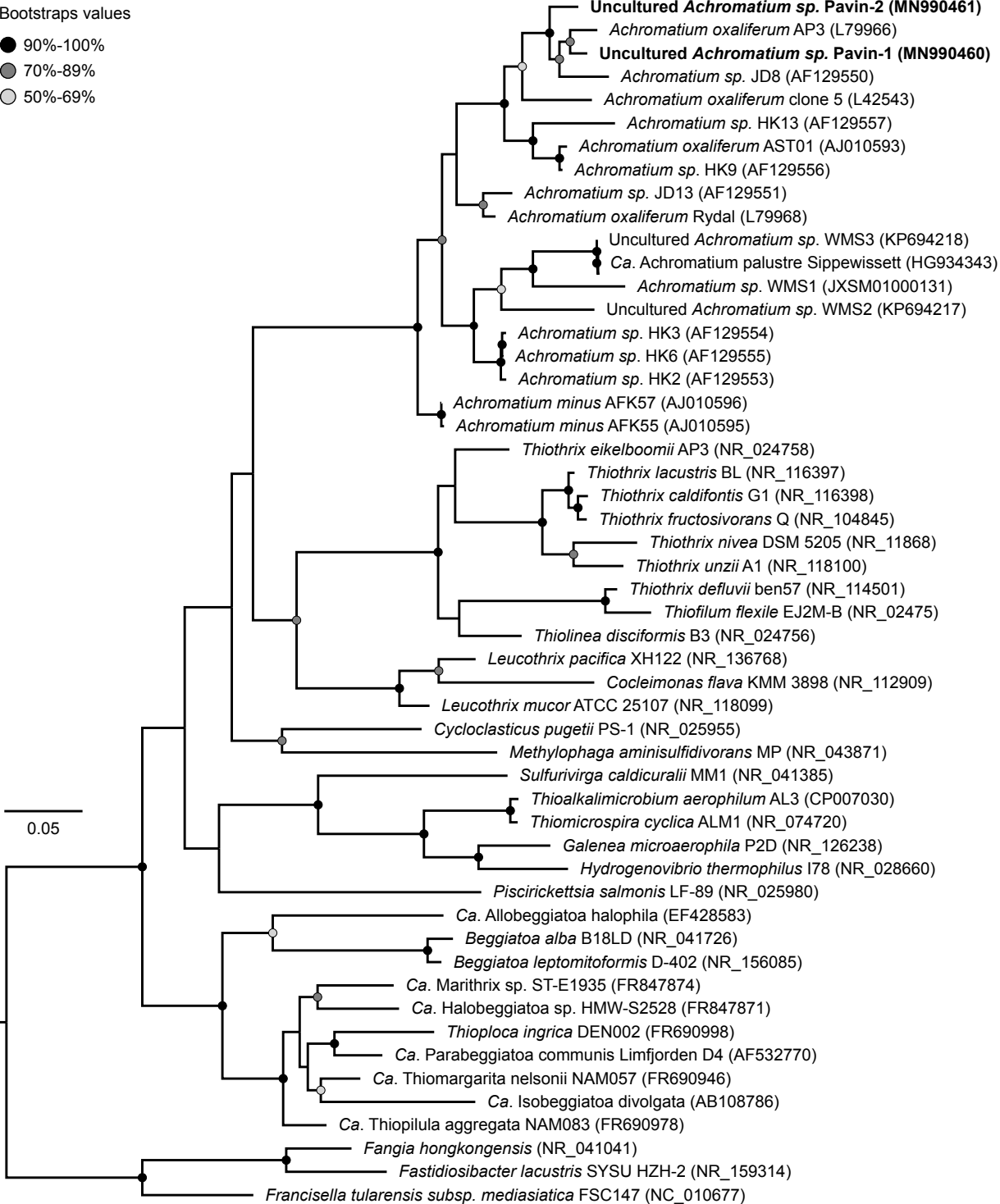
314

Bootstraps values

● 90%-100%

● 70%-89%

○ 50%-69%



315 **Figure 2:** Maximum likelihood phylogenetic tree of the Thiotrichaceae and Pisciricettsiaceae
316 families based on the 16S rRNA gene sequences showing the evolutionary relationships
317 between the two CaCO₃-accumulating isolates from Lake Pavin (Pavin-1 and Pavin-2) and their
318 *Achromatium* relatives. The tree was built with the maximum likelihood method and the
319 GTRGAMMAI substitution model. *Fangia hongkongensis*, *Fastidiosibacter lacustris* and
320 *Francisella tularensis* subsp. *mediasiatica* were used as an outgroup. The tree was drawn to
321 scale and branches length represents the number of base substitutions per site. Only bootstrap
322 values above 50% are shown and annotated to a circle.

323

324

325

326

327

328

329

330

331

332

333

334

335

336

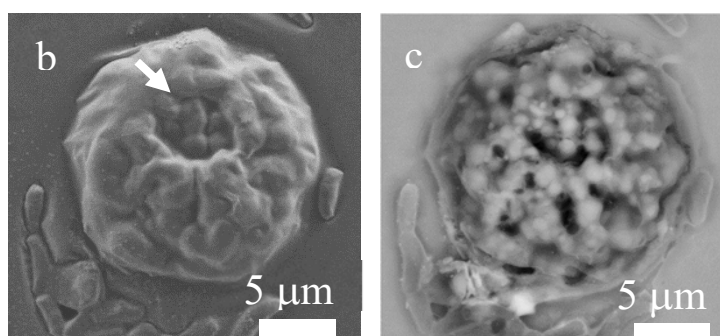
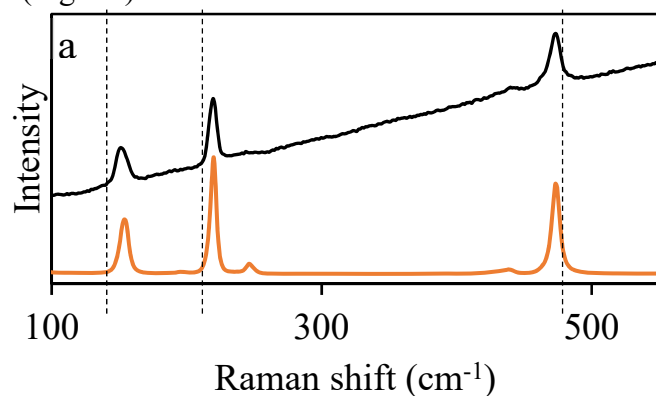
337

338

339

340 Raman spectroscopy analyses were conducted on seven *Achromatium* cells sorted from the
341 sediments by micromanipulation. Several spots were analyzed for each cell. Then, cells were
342 systematically relocated and imaged by SEM and their elemental chemical composition mapped
343 by SEM-EDXS.

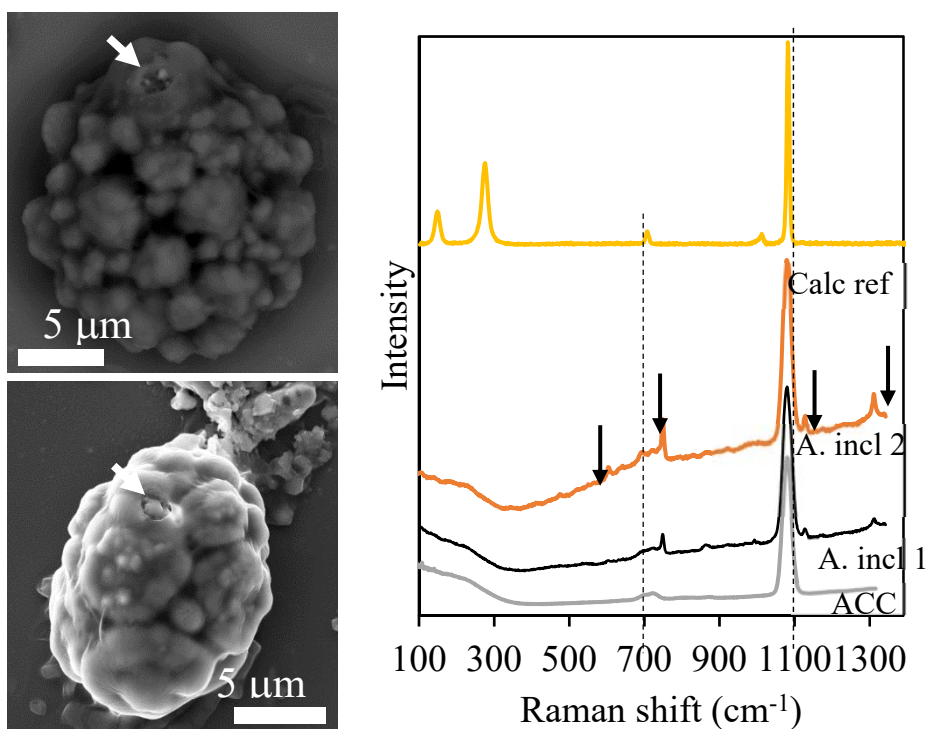
344 One of the 7 cells showed a particular Raman spectrum with major peaks at 150.8, 219.7 and
345 473.5 cm^{-1} (Figure 3). This spectrum was identical to the spectrum referred to as biosulfur by
346 Nims et al. (2019), consisting of elemental sulfur inclusions in bacteria. Consistently with what
347 was reported by these authors, the three observed peaks were unambiguously assigned to
348 asymmetric S-S bending, symmetric S-S bending and S-S bond stretching of a S_8 ring structure,
349 respectively. Consistently, SEM-EDXS mapping showed that this cell contained numerous S-
350 rich inclusions (Fig. S1).



361 **Figure 3:** (a) Raman spectrum of an *Achromatium* cell with sulfur inclusions. The top black
362 spectrum is obtained on the *Achromatium* cell shown in the SEM images. The bottom orange
363 spectrum was issued from the RUFF database and was measured on elemental sulfur
364 (#R040135). Vertical dashed lines indicate peaks at 150.8, 219.7 and 473.5 cm^{-1} . (b) SEM
365 image of the analyzed *Achromatium* cell were measured in the secondary electron mode (SE2;
366 left) with an accelerating voltage of 2 keV. The white arrow indicates the approximate location
367 where a low power Raman analysis was performed. (c) SEM image of the same cell shown in
368 (b), observed in the backscattered electron mode (ASB; right) with an accelerating voltage of
369 15 keV.

370 On 5 cells out of 7, Raman spectra measured with 1% of the maximum laser power were similar
371 to those shown in Figure 4. These spectra showed two sets of peaks: a first set comprised four
372 peaks at 604, 749.4, 1128 and 1311.3 cm^{-1} . Based on Pätzold et al. (2008), these peaks were
373 assigned to the ν_{24} , ν_{15} , ν_{22} and ν_{21} modes of a porphyrin ring in cytochromes. Interestingly,
374 these bands disappeared upon prolonged irradiation (Fig. S2). The second set comprised a very
375 broad peak, likely the convolution of two broad peaks, extending between 681 and 752 cm^{-1}
376 and another broad peak centered, depending on the spectra, between 1079.45 and 1082.43 cm^{-1}
377 ¹. These peaks were identical to those of an amorphous calcium carbonate (ACC) reference
378 spectrum (Figure 4). The very broad band between 681 and 752 cm^{-1} was assigned to the in-
379 plane bend (ν_4) of C-O bonds. The strong and broad peak at around 1079.9 cm^{-1} corresponded
380 to the symmetric stretching of C-O bonds in carbonate groups (ν_1 peak) in a CaCO_3 phase. This
381 assignment to ACC was further supported by the absence of sharp peaks characteristic of lattice
382 mode vibrations in crystalline CaCO_3 phases below 400 cm^{-1} . Instead, we observed a single
383 broad bump between the cutoff at ~ 50 nm and ~ 400 nm (Figure 4). Accordingly, SEM-EDXS
384 analyses showed that these cells were rich in Ca with a minor EDXS peak of Mg, the relative
385 height of which varied from one cell to another (Fig. S1).

386
387
388
389
390
391
392
393
394



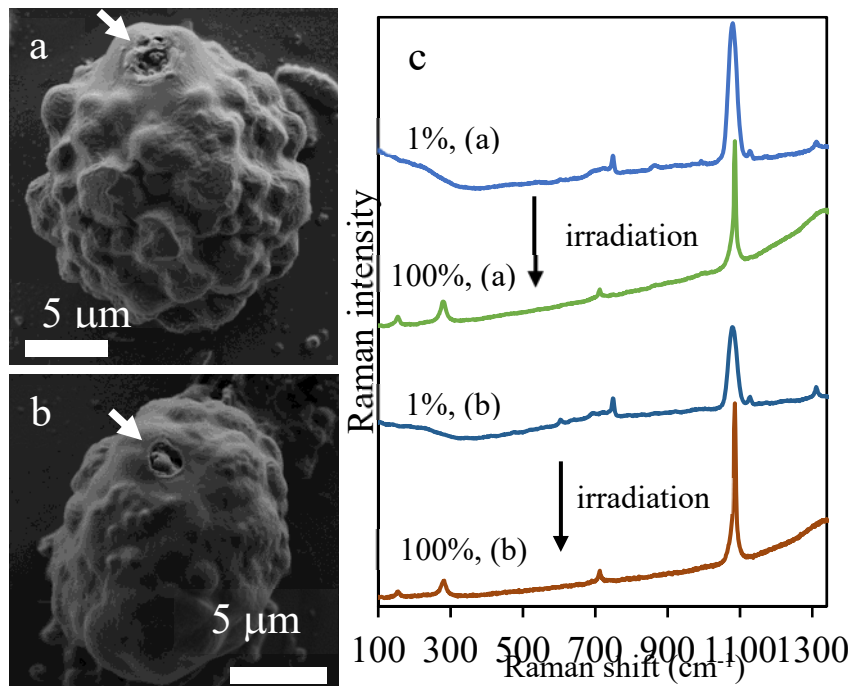
395 **Figure 4:** (Left) SEM images of the cells on which the Raman spectra were measured. White
396 arrows indicate where full power Raman analyses were performed. (Right) Raman spectra. The
397 two middle spectra (A. incl 1 and 2) are Raman spectra of CaCO₃ inclusions in *Achromatium*
398 cells. The two dashed lines show (i) a broad band between 681 and 752 cm⁻¹, assigned to the
399 in-plane bend (ν_4) of C-O bonds in ACC and (ii) a broad band around 1079.9 cm⁻¹ assigned to
400 the symmetric stretching (ν_1) of C-O bonds in carbonate groups in ACC. Arrows show bands
401 at 604.2, 749.4, 1127.9 and 1311.3 cm⁻¹, assigned to the ν_{24} , ν_{15} , ν_{22} and ν_{21} modes of a
402 porphyrin ring in cytochromes. The top spectrum (Calc ref) is a Raman spectrum of a reference
403 calcite crystal retrieved from the RUFF database (#R040170). The bottom spectrum (ACC ref)
404 is a Raman spectrum of a synthetic reference ACC particle.
405

406 When full laser power was used, the spectra measured on *Achromatium* intracellular granules
407 changed and eventually showed very different spectral features (Figure 5 and Figure 6). First,
408 two Raman bands appeared at ~154 and 280 cm⁻¹ after irradiation. These bands were
409 unambiguously assigned to the translation and higher frequency libration modes in calcite and
410 were due to collective synchronized vibrations of atoms around their equilibrium positions
411 (Perrin et al., 2016). The very broad ν_4 band of ACC was replaced by a narrow band at 712.2
412 cm⁻¹ that was consistently assigned to the ν_4 mode of calcite. The broad band at ~1079.9 cm⁻¹
413 of ACC was replaced by a narrower band at ~1086 cm⁻¹, also consistently assigned to ν_1 in
414 calcite. Last, the Raman bands at 604, 749.4, 1128 and 1311.3 cm⁻¹ of cytochromes, associated
415 with ACC, were absent from the calcite spectra. SEM pictures at low voltage of the cells where
416 this transformation was observed showed that they were systematically enveloped by a cell
417 wall, detected here as an envelope opaque to low energy electrons and therefore preventing the
418 direct visualization of the granules inside the cells (Figures 4-6). In contrast, when the cell wall
419 was disrupted, one could visualize directly the intracellular CaCO₃ granules, as shown in Figure
420 6. Local damages induced by the laser spot could be observed as a crater measuring ~2 μm in
421 diameter (Figure 5b). In one case, the cell partly disrupted and the irradiated calcite residue was
422 extruded from the cell. The resulting byproduct showed a granular microtexture (Figure 6).

423

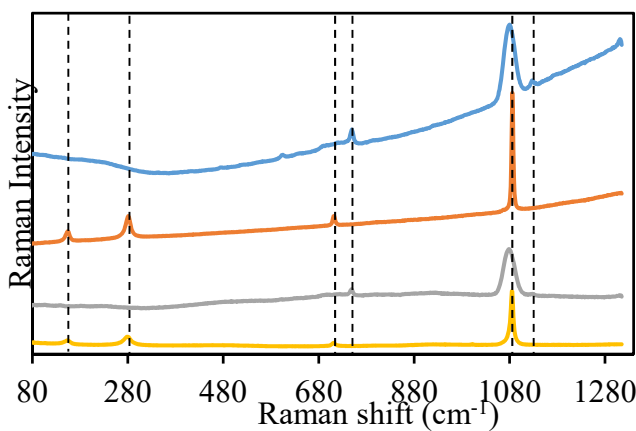
424

425
426
427
428
429
430
431
432
433

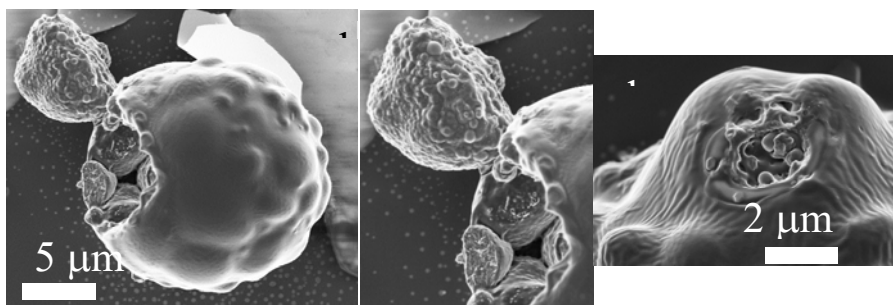


434 **Figure 5:** (a) and (b) SEM images acquired at 2 keV in the secondary electron mode showing
435 the *Achromatium* cells analyzed by both Raman and SEM. Arrows show the irradiation spots
436 where ACC transformed into calcite following full laser power irradiation. (c): Raman spectra
437 obtained using 1% and 100% laser power on cells shown in (a) and (b). Dashed lines are located
438 at ~154, 280, 604, 712.2, 749.4, 1079.9, 1127.9 and 1311.3 cm⁻¹.
439

440
441
442
443
444
445



446
447
448
449



450 **Figure 6:** (a) Raman spectra of ACC granules in 2 *Achromatium* cells obtained by low laser
451 power irradiation (blue and grey spectra), before transformation into calcite after full laser
452 power irradiation (orange and yellow). Dashed vertical lines are located at ~154, 280, 712.2,
453 749.4, 1079.9, and 1127.9 cm⁻¹. (b) SEM image obtained at 2 keV by the InLens detector. A
454 fragment was partly detached from the cell on the top left after laser irradiation. (c) Close-up

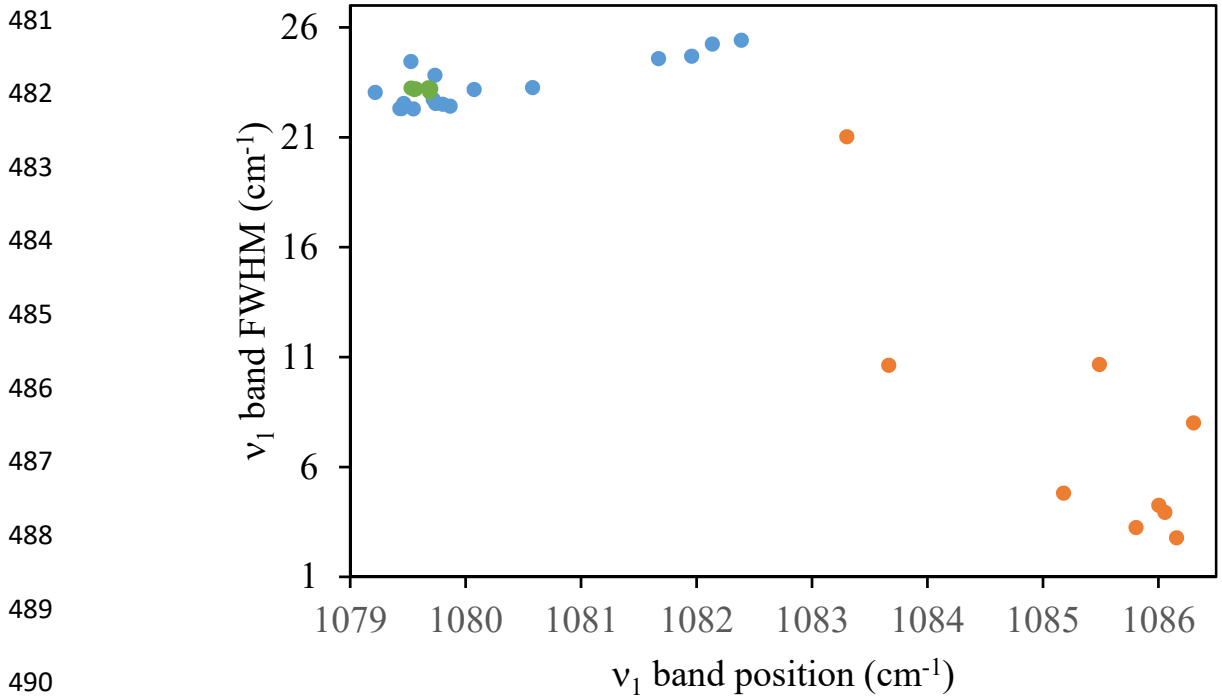
455 of the detached fragment showing the granular texture of calcite in the extruded fragment vs
456 smooth texture in ACC within the cells. (d) Close-up of the crater induced by laser in another
457 *Achromatium* cell and showing the texture of the transformed area.

458

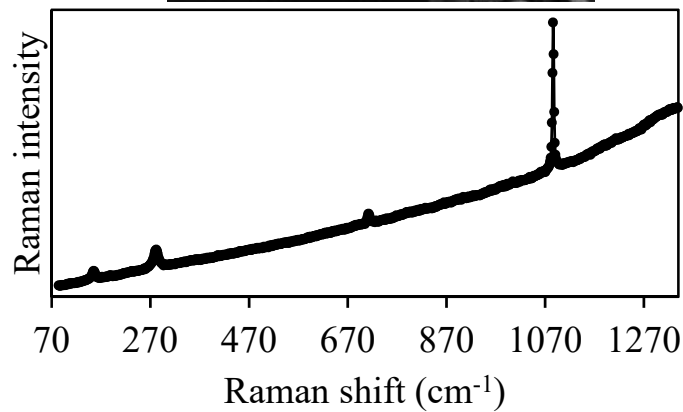
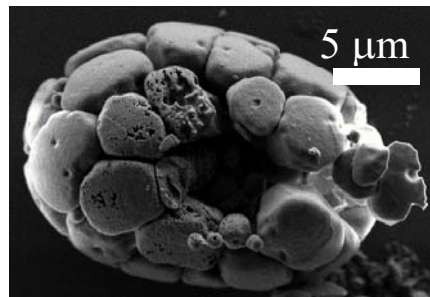
459 The ν_1 band of *Achromatium* CaCO_3 granules irradiated at low laser power (from 1 to 10% of
460 the total power) and full laser power were systematically fitted. In most cases, a very good fit
461 was obtained using one Voigt function but for several spectra measured after strong irradiation,
462 the ν_1 band was clearly asymmetric and best fitted with two Voigt functions (Fig. S3). When
463 plotting the ν_1 band position vs the full width at half maximum (FWHM) of the Lorentzian
464 profile, a clear difference was observed between weakly (0.1-10% of the maximum laser power)
465 vs strongly (100% of the maximum laser power) irradiated granules, further highlighting the
466 transformation of ACC into calcite upon irradiation (Figure 7). The FWHM for weakly
467 irradiated synthetic and *Achromatium* ACC varied between 24.9 and 28.6 cm^{-1} and was
468 positively correlated with the band position, which varied between ~ 1079.5 and 1082.4 cm^{-1} .
469 In contrast, the FWHM for all strongly irradiated *Achromatium* ACC were between 24.7 down
470 to 2.5 cm^{-1} which negatively correlated with the band positions, varying between 1082.4 and
471 1086.3 cm^{-1} . The components with higher FWHM/lower position were minor fit components
472 of asymmetric bands and were interpreted as poorly crystalline remnants mixed with more
473 crystalline components in irradiated zones similarly to what was shown by Wehmeister et al.
474 (2011) (Figure 7).

475 In the case of one *Achromatium* cell, the Raman spectrum measured with 1% of the maximum
476 laser power was very similar to that of the most irradiated *Achromatium* granules and to that of
477 calcite with bands at $\sim 154, 280, 712.2$ and 1086.2 cm^{-1} (Figure 8). SEM observations performed
478 at low voltage showed that this cell was devoid of a cell wall on the contrary to the cells
479 containing ACC as mentioned before.

480



490 **Figure 7:** Scatterplot showing the full width at half maximum (FWHM) versus the position for
 491 the ν_1 Raman band of the CaCO_3 phase. Blue dots correspond to Raman spectra measured on
 492 *Achromatium* CaCO_3 inclusions with reduced laser power (1 or 5 %). Green dots correspond to
 493 Raman spectra measured on synthetic reference ACC grains with reduced laser power (1 or 5
 494 %). Orange dots correspond to Raman spectra measured on *Achromatium* CaCO_3 inclusions
 495 with full laser power and showing signs of crystallization.
 496



507 **Figure 8:** (a) SEM images acquired at 2 keV in the secondary electron mode showing an
 508 *Achromatium* cell analyzed by both Raman at 1% laser power and SEM. (b): Raman spectrum
 509 obtained using 1% laser power on the cell shown in (a). Dashed lines are located at ~ 154 , 280,
 510 712.2 and 1086.2 cm^{-1} and underline bands that are characteristic of calcite.
 511

512 4. Discussion

513

514 4.1. Precautions to be taken in order to assess the crystallinity of CaCO₃ in *Achromatium* 515 cells

516

517 The present data clearly show that the CaCO₃ granules in Lake Pavin *Achromatium* intact cells
518 are composed of ACC and not calcite. Only one cell contained calcite granules but SEM
519 observations suggested that this cell was damaged since it did not show any cell wall as
520 discussed below. Several studies have detailed how Raman spectroscopy could unambiguously
521 discriminate between ACC and calcite (e.g., DeCarlo, 2018). This includes the presence (in
522 calcite)/absence (in ACC) of lattice modes at ~154 and 280 cm⁻¹; a sharp (calcite) vs wide
523 (ACC) ν_1 peak. The latter feature has been explained as the result of a high variability in the
524 bonding environment around the carbonates in ACC which causes deviations in the lengths of
525 C–O bonds. Last, a shift in the ν_1 peak position from lower (ACC) to higher (calcite)
526 wavenumbers is observed. Wang et al. (2012) and Perrin et al. (2016) showed that variations in
527 the Mg content of ACC and calcite could change in a correlated manner with the FWHM and
528 position of the ν_1 peak. Accordingly, we observed in our study some correlated variations in
529 the FWHM and peak position of the ν_1 peak in ACC granules, with variation of FWHM in the
530 22.5-25.4 cm⁻¹ range, which according to Wang et al. (2012) may be explained by variations in
531 their Mg contents in the 0-10% range. Perrin et al. (2016) also noticed that (1) the FWHM of
532 calcite and ACC, whatever their Mg content, did not overlap, and (2) ν_1 wavenumbers lower
533 than 1086 cm⁻¹ and ν_1 FWHM greater than 22 cm⁻¹ were two unambiguous criteria to determine
534 the amorphous nature of calcium carbonate. Therefore, it can be confidently concluded that
535 Raman spectra collected on most Lake Pavin *Achromatium* cells were characteristic of ACC.
536 This conclusion fully agrees with the early studies by West and Griffiths (1913) who suggested
537 that intracellular granules in *Achromatium* were composed of a colloidal form of CaCO₃ and

538 later on by Bersa (1926) who mentioned amorphous CaCO₃ (“amorphen (kolloidalen) Form”
539 in their manuscript). It also better explains Yang et al. (2019)’s FIB observations of composite
540 structure of the granules with submicrometer laminations, which would be difficult to explain
541 within a single crystal, as mentioned by the authors themselves. Similar laminations in ACC
542 granules, attributed to chemical variations, were observed by TEM by Martignier et al. (2017)
543 (2017) and Cam et al. (2016).

544 We note that several artefacts may lead to an erroneous assessment of the crystallinity of
545 *Achromatium* CaCO₃ granules. First, in a population of *Achromatium* cells, some ACC granules
546 may transform into calcite because of, e.g., cell death and/or sample preparation. Indeed, it has
547 been emphasized by many authors (e.g., Gower, 2008; Politi et al., 2006) that ACC is usually
548 unstable and often converts to a crystalline phase during sample preparation of biominerals for
549 *ex vivo* examinations. Consistently, a spontaneous transformation of ACC into calcite was
550 documented by the early observations by West and Griffiths (1913) and Bersa (1926) when
551 they killed the cells by adding alcohol or drying. Schorn et al. (2020) observed dissolution of
552 *Achromatium* ACC granules when they treated cells with acids. In the meantime, Schorn et al.
553 (2020) sometimes evidenced some crystallization when killing them with no acidification of
554 the solution. In the present study, while we observed that simple drying does not induce
555 crystallization of ACC, we observed one cell containing calcite. On the contrary to other cells,
556 this one lacked a cell wall. We cannot affirm whether the cell wall was already disrupted in the
557 sample before micromanipulation or if it occurred upon sample preparation but as mentioned
558 above, this explains why ACC granules transformed into calcite in this cell before Raman
559 analyses.

560 Second, in addition to sample preparation, irradiation at too high laser power can also cause
561 ACC crystallization as shown in the present study. This transformation may result from the
562 local heating of ACC in the laser spot over ~330°C, a temperature at which the solid-solid

563 transformation of ACC into calcite is detected by thermogravimetric analyses (Fig. S4). Such a
564 local increase of T may result from a high absorption of light by, e.g., cytochromes, which
565 contribute to the Raman signal of *Achromatium* cells and efficiently absorb visible light at ~530
566 nm (Okada et al., 2012) and a slow dissipation of the heat in the material (Fau et al., 2019). As
567 shown by Fau et al. (2019), a more precise assessment of the temperature increase induced by
568 laser heating would require the knowledge of the optical penetration depth and thermal
569 penetration depth in organics-containing ACC granules, which we do not know yet.

570 An alternative interpretation of these observations could consist in suggesting that only a
571 surficial layer of the *Achromatium* granules was illuminated and therefore heated by the laser.
572 This surficial layer would be an ACC layer covering an initially unseen calcite core. This
573 initially unseen calcite core may then become apparent after volatilization of the ACC layer.
574 However, this interpretation is unlikely for two reasons. First, this would mean that ACC is
575 quite opaque. While we do not know the value of the optical penetration depth as mentioned
576 above, Schmidt and Wagermeier (2017) reported that cystoliths in plants, composed of ACC
577 and measuring 40-60 μm function as light scatterers due to their transparency to visible light.
578 This suggests that green Raman light likely propagates throughout the 3-4 μm wide ACC
579 granules of *Achromatium*. Second, if a surficial layer of ACC was volatilized (after
580 crystallization into calcite at ~330°C), this would produce CaO, which we did not detect by
581 Raman.

582 Overall, the high susceptibility of ACC to transform into calcite upon cell death and/or sample
583 preparation and/or laser irradiation concurs to the assumption made by Gower (2008) that this
584 explains why it took so long to discover ACC although it is common. This applies well to
585 *Achromatium* too. Two studies produced data suggesting a calcitic nature of the CaCO_3 granules
586 in *Achromatium* using bulk x-ray diffraction (Head et al., 2000) and Raman spectroscopy
587 (Salman et al., 2015). However, XRD is much more sensitive to calcite than ACC and therefore

588 even in a bulk sample where most of the cells contain ACC and only a few dead ones contain
589 calcite, the latter signal would show up. Salman et al. (2015) analyzed *Achromatium* cells by
590 Raman spectroscopy and obtained one spectrum typical of calcite. However, they did not
591 mention the use of neutral density filters and may have acquired Raman spectra at full laser
592 power. Alternatively, morphologically and genetically distinct subpopulations of *Achromatium*
593 have been evidenced in several localities, although this idea was challenged by recent studies
594 that instead suggested variations in gene expression across varying environments (Ionescu et
595 al., 2020). One may postulate that some *Achromatium* populations may produce calcite instead
596 of ACC. Moreover, the *Achromatium* populations studied by Salman et al. (2015) thrived in a
597 salt marsh which is chemically very different from the freshwater of Lake Pavin. While it is not
598 clear how salinity may directly impact the stability of ACC, it is possible that environmentally-
599 driven variations in ion homeostasis in cells result in different chemical environments around
600 CaCO₃ granules. Similarly, one may wonder if *Achromatium minus* thriving in the more acidic
601 lake Fuchskuhle (pH=4.2-4.6) (Glöckner et al., 1999) may form calcite instead of ACC.
602 Overall, only future systematic studies will be able to decipher if intracellular CaCO₃ granules
603 in *Achromatium* living cells are always composed of ACC or sometimes calcite. The present
604 study offers guidelines to avoid potential artifacts including the use of low Raman laser
605 irradiation (preferably <1 mW for a 532 nm laser), then SEM to verify that the cell wall is still
606 enveloping the cells. It is possible that air-drying induces some damages in some cases and that
607 high-pressure freeze-substitution sample preparation may overcome this issue (Blondeau et al.,
608 2018) but this will have to be tested by future studies.

609 **4.2. What makes bacteria producing intracellular ACC instead of intracellular calcite?**

610

611 ACC are notoriously unstable phases (e.g., Addadi et al., 2003; Cavanaugh et al., 2019).
612 Therefore, it may appear surprising that *Achromatium*, a magnetotactic alphaproteobacterium
613 and cyanobacteria manage to preserve CaCO₃ as ACC intracellularly, and that it does not

614 transform into a crystalline phase such as calcite. In any case, the mechanism involved in this
615 stabilization appears to no longer operate as soon as the cells lyse/die explaining why in this
616 case ACC spontaneously crystallizes as reported here and by previous studies.

617 Laboratory biomimetic experiments showed that several chemical species can stabilize ACC at
618 least transiently, such as magnesium ions, triphosphate ions, polymers such as diphosphate-
619 substituted poly(ethylene glycol) and polyaspartate, polyphosphonates, some oligosaccharides
620 or amino acids (Addadi et al., 2003; Zou et al., 2020). It is clear that at least some of these
621 chemical species are abundant within the cell environment and may, therefore, play a role in
622 ACC stabilization. However, how they may degrade and hence stop from stabilizing ACC when
623 the cells disrupt remains to be understood. Alternatively, the stabilization of ACC may well be
624 explained by confinement as demonstrated by, e.g. Zeng et al. (2018) and Cavanaugh et al.
625 (2019). Based on microfluidics experiments, Cavanaugh et al. (2019) concluded that ACC is
626 the expected byproduct of intracellular biomineralization occurring within a micrometer-sized
627 compartment when the solution in this compartment is supersaturated with ACC. Moreover,
628 they predict that ACC may remain stable for durations much longer than the lifetime of the
629 organisms, i.e, months before crystallization occurs in 1% of $10 \mu\text{m}^3$ vesicle and hundred years
630 before it occurs in 99% of it. According to Jin et al. (2018), confinement can be seen as a barrier
631 to water diffusion, which hinders the dissolution of ACC and reprecipitation as calcite. In
632 cyanobacteria forming intracellular ACC, it has been shown that this confinement may be
633 provided by an organic envelope of a yet-unknown composition (Blondeau et al., 2018). We
634 presently do not know the genes or proteins involved in the formation of this organic envelope.

635 In *Achromatium* and the recently discovered magnetotactic alphaproteobacterium, it has been
636 suggested that ACC granules are confined by lipid bilayers (N. Gray & Head, 2014; Monteil et
637 al., 2020). It can be speculated that such envelopes may also control the maximum size of the
638 granules as observed for example in magnetotactic bacteria and prevent their agglomeration but

639 this will need further assessment in the future. Cavanaugh et al. (2019) noticed that when the
640 confinement was broken, the exposition of ACC to heterogeneous nucleators induced rapid
641 crystallization. Moreover, Liu et al. (2020) explained how this transformation of ACC into
642 calcite by dissolution-reprecipitation could preserve the morphology of the granules by
643 occurring without the need to nucleate a separate crystal. How the envelopes of ACC granules
644 in cyanobacteria and *Achromatium* rupture will need to be further studied. For this purpose,
645 TEM appears as the choice method since Raman microspectroscopy does not offer a spatial
646 resolution high enough to detect such an organic envelope.

647 Overall, intracellular compartmentalization by lipid bilayers or proteins seems required to
648 explain the formation and stabilization of ACC. This contradicts the recent suggestion by
649 Schorn et al. (2020) that CaCO₃ in *Achromatium* cells would be in contact with the extracellular
650 environment and form in pockets delimited by an invagination of the cytoplasmic membrane
651 and would, therefore, be periplasmic. We note that these conclusions by Schorn et al. (2020)
652 were not derived from direct observations of the ACC granules within these pockets by, e.g.
653 TEM tomography. Instead, they were postulated based on 1) the idea that the easy loss of
654 CaCO₃ upon various physico-chemical treatments is consistent with the fact that they would
655 not be membrane enclosed; and 2) the fact that fluorescein, a hydrophilic dye that does not
656 penetrate membranes, did penetrate inside cavities hosting CaCO₃. However, several other facts
657 may oppose Schorn et al. (2020) conclusion. First, ACC granules in cyanobacteria are also
658 easily and rapidly lost upon various physico-chemical treatments and yet they clearly form
659 within intracellular enclosed compartments (Blondeau et al., 2018). The chemicals used by
660 Blondeau et al. (2018), i.e. ethanol which is membrane permeable, are not the same as those
661 used by Schorn et al (2020), i.e. HCl, which is membrane impermeable. Yet both chemical may
662 harm/stress the cells and induce intracellular changes. Second, Bentov et al. (2009) similarly
663 observed that calcein, another membrane-impermeable dye as these authors underline it, did

664 stain the truly intracellular CaCO₃ of foraminifera. Last, the suggestion that CaCO₃ in
665 *Achromatium* would be in direct contact with the extracellular environment is inconsistent with
666 the report of ACC formation by some *Achromatium* cells in environmental solutions
667 undersaturated with ACC (Gray & Head, 2014).

668

669 **4.3. Implications of an ACC instead of a calcitic composition of intracellular granules**

670 There are several important ecological, geological and ultrastructural implications in reporting
671 that *Achromatium* intracellular granules are composed of ACC and not calcite.

672 First, several studies have discussed the potential function(s) of *Achromatium* CaCO₃ granules
673 (e.g., Gray & Head, 2014; Salman et al., 2015; Schorn et al., 2020; Yang et al., 2019). The
674 dominant view emerging lately suggests that these granules buffer intracellular pH, which may
675 otherwise vary due to the redox transformations of S species. It has been noted that for this
676 purpose the cells need to quickly adjust their CaCO₃ content to rapidly changing environmental
677 conditions, such as exposure to O₂ (Yang et al., 2019). We argue that this can be better explained
678 by ACC than calcite. Addadi et al (2003) and Weiner et al. (2005) consistently suggested that
679 ACC is a widespread biomineral phase and holds a homeostatic function in eukaryotes which
680 is facilitated by its metastability. Moreover, while the reactivity of calcite and ACC (e.g., the
681 kinetics of precipitation or dissolution) depends on prevailing chemical conditions, it has been
682 shown that under given conditions, ACC reactivity might be higher, partly because of a higher
683 surface area (Lassin et al., 2018). Altogether, these arguments support the idea that ACC may
684 respond more quickly to chemical changes than calcite and therefore fill such a buffering
685 function with a higher efficiency.

686 A second implication results from the solubility difference between ACC and calcite. Although
687 there remains some uncertainty about the exact value of the solubility of ACC, it is much higher,
688 at least one order of magnitude than that of calcite (Brečević & Nielsen, 1989; Carino et al.,

689 2017; Purgstaller et al., 2019). Solubility of ACC is even higher when its Mg content increases
690 (Purgstaller et al., 2019). This means that ACC precipitation requires a higher activity of Ca^{2+}
691 and/or a higher activity of HCO_3^- and/or a higher pH within the compartment where it forms. It
692 also means that ACC starts dissolving under conditions where calcite would still be stable. The
693 chemical composition inside the compartments where granules form is not known but future
694 modelling efforts aiming at inferring the chemical conditions prevailing in these compartments
695 should take into account the fact that these granules are composed of ACC and not calcite.

696 As a third implication, Bolze et al. (2002) reported densities of 1.62 and 2.75 g/cm^3 for hydrated
697 ACC and calcite, respectively. Fernandez-Martinez et al. (2013) measured a density of 2.18
698 g/cm^3 for dry ACC powder which remains significantly lower than that of calcite. This means
699 that when ACC crystallizes to calcite, this represents a volume variation between 20 to 40%.

700 This suggests that when ACC crystallizes to calcite in dying cells, one should expect a reduction
701 in size of the granules, unless further *post-mortem* crystal growth occurs. Moreover, it has been
702 hypothesized by some authors that intracellular granules in *Achromatium* are used to regulate
703 buoyancy of the cells (Gray, 2006). While ACC-filled cells remain denser than ACC free cells,
704 they are lighter than calcite-filled cells and therefore this role for increasing cell buoyant density
705 would be less efficient with ACC than calcite. Last, Mansor et al. (2015) noted that the
706 precipitation of CaCO_3 within cells generates H^+ and assumed that these protons may be used
707 to generate ATP. They used for their calculations the density of calcite to estimate the average
708 amount of Ca stored in cells which they equaled to the amount of CO_3^{2-} stored into the granules
709 and from there inferred the equivalent amount of generated protons. Here we note that these
710 calculations should be revised; using ACC density will decrease these numbers by at least 20
711 to 40%. We also note an additional difficulty for these calculations: first Mg substitution should
712 be taken into account since it impacts the density of the ACC phase. Then, on the contrary to
713 calcite, the $\text{Ca}:\text{CO}_3^{2-}$ stoichiometry is not always 1:1 in ACC as there can be some HCO_3^-

714 molecules as well, the proportion of which may depend on pH and temperature conditions
715 (Carino et al., 2017). Those should not be counted to infer the equivalent proton amount. The
716 advent of future experimental approaches e.g. measuring intracellular ATP *in vivo* will be
717 essential to test these calculations.

718 Last, as mentioned above, the stability of ACC is lower than that of calcite. Therefore, even if
719 ACC granules remain confined after the death of the cells, one may not expect to find genuine
720 ACC in the geological record. Indeed, Cavanaugh et al (2019) showed that confined ACC
721 granules measuring $\sim 1 \mu\text{m}^3$ would be preserved from crystallization up to about one million
722 years. Therefore, a fossil of an ACC granule would be a crystalline phase, most likely calcite.
723 In order to understand how to look for some potential traces of these ACC granules in the
724 geological record, it will be important to decipher in the future: 1) what conditions are prone to
725 crystallization of ACC in calcite; 2) if the morphology of ACC granules is always preserved
726 upon crystallization; and 3) if the crystallized granules replacing ACC store some organic
727 molecules that might be present in ACC granules and/or if a particular trace element
728 composition is preserved.

729

730 **5. Conclusion**

731 We find robust evidence that cells of the giant gammaproteobacterium *Achromatium* sp. in Lake
732 Pavin form intracellular ACC and not calcite. In contrast, previous reports of calcite may have
733 been affected by the high instability of ACC, which transforms readily into calcite upon some
734 sample treatments, which alter the integrity of the cells, or strong laser irradiation. Raman
735 microspectroscopy seems to be the most appropriate tool to infer the ACC nature of these
736 inclusions since analyses can be conducted under native conditions. However, special care has
737 to be taken to minimize irradiation delivered to the cells and check that cells are still covered
738 by a wall. Moreover, we advocate that future studies should prefer the term CaCO_3 to calcite or

739 ACC if they did not characterize the crystallinity of the intracellular granules. Reporting that
740 ACC instead of calcite is the constituent of CaCO₃ granules in *Achromatium* cells does not
741 enlighten the mechanisms of formation of these granules. However, it sets new constraints on
742 them such as the requirement of a confinement and the need for a higher saturation level of the
743 solution in which CaCO₃ forms. It also modifies the quantitative impact of these biominerals
744 on the physiology of the cells. Last, Jin et al. (2018) highlighted that ACC is widespread in
745 biomineralizing eukaryotes. Here we show that this is also the case in prokaryotes since the
746 presently three known cases of intracellular biomineralization in bacteria, i.e. diverse
747 cyanobacteria, some magnetotactic Alphaproteobacteria and *Achromatium*, all form ACC.

748

749

750

751 **References**

752 Addadi, L., Raz, S., & Weiner, S. (2003). Taking Advantage of Disorder : Amorphous Calcium

753 Carbonate and Its Roles in Biomineralization. *Advanced Materials*, 15(12), 959-970.

754 <https://doi.org/10.1002/adma.200300381>

755 Babenzien, H.-D. (1991). *Achromatium oxaliferum* and its ecological niche. *Zentralblatt Für*

756 *Mikrobiologie*, 146(1), 41-49. [https://doi.org/10.1016/S0232-4393\(11\)80258-1](https://doi.org/10.1016/S0232-4393(11)80258-1)

757 Babenzien, H.-D., Glöckner, F. O., & Head, I. M. (2015). *Achromatium*. In W. B. Whitman, F. Rainey, P.

758 Kämpfer, M. Trujillo, J. Chun, P. DeVos, B. Hedlund, & S. Dedysh (Éds.), *Bergey's Manual of*

759 *Systematics of Archaea and Bacteria* (p. 1-8). John Wiley & Sons, Ltd.

760 <https://doi.org/10.1002/9781118960608.gbm01222>

761 Behrens, G., Kuhn, L., Uvic, R., & Heuer, A. (1995). Raman-Spectra of Vateritic Calcium-Carbonate.

762 *Spectroscopy Letters*, 28(6), 983-995. <https://doi.org/10.1080/00387019508009934>

763 Bentov, S., Brownlee, C., & Erez, J. (2009). The role of seawater endocytosis in the biomineralization
764 process in calcareous foraminifera. *Proceedings of the National Academy of Sciences*,
765 *106*(51), 21500-21504. <https://doi.org/10.1073/pnas.0906636106>

766 Benzerara, K., Skouri-Panet, F., Li, J., Ferard, C., Gugger, M., Laurent, T., Couradeau, E., Ragon, M.,
767 Cosmidis, J., Menguy, N., Margaret-Oliver, I., Tavera, R., Lopez-Garcia, P., & Moreira, D.
768 (2014). Intracellular Ca-carbonate biomineralization is widespread in cyanobacteria.
769 *Proceedings of the National Academy of Sciences*, *111*(30), 10933-10938.
770 <https://doi.org/10.1073/pnas.1403510111>

771 Bersa, E. (1926). Über das Vorkommen von kohlensaurem Kalk in einer Gruppe von
772 Schwefelbakterien. *Berichte Der Deutschen Botanischen Gesellschaft*, *44*(7), 474-478.
773 <https://doi.org/10.1111/j.1438-8677.1926.tb00996.x>

774 Blondeau, M., Sachse, M., Boulogne, C., Gillet, C., Guigner, J.-M., Skouri-Panet, F., Poinot, M.,
775 Ferard, C., Miot, J., & Benzerara, K. (2018). Amorphous Calcium Carbonate Granules Form
776 Within an Intracellular Compartment in Calcifying Cyanobacteria. *Frontiers in Microbiology*,
777 *9*, 1768. <https://doi.org/10.3389/fmicb.2018.01768>

778 Bolze, J., Peng, B., Dingenouts, N., Panine, P., Narayanan, T., & Ballauff, M. (2002). Formation and
779 growth of amorphous colloidal CaCO₃ precursor particles as detected by time-resolved SAXS.
780 *Langmuir*, *18*(22), 8364–8369.

781 Brečević, L., & Nielsen, A. E. (1989). Solubility of amorphous calcium carbonate. *Journal of Crystal*
782 *Growth*, *98*(3), 504-510. [https://doi.org/10.1016/0022-0248\(89\)90168-1](https://doi.org/10.1016/0022-0248(89)90168-1)

783 Cam, N., Benzerara, K., Georgelin, T., Jaber, M., Lambert, J.-F., Poinot, M., Skouri-Panet, F., &
784 Cordier, L. (2016). Selective uptake of alkaline earth metals by cyanobacteria forming
785 intracellular carbonates. *Environmental Science & Technology*, *50*(21), 11654-11662.
786 <https://doi.org/10.1021/acs.est.6b02872>

787 Carino, A., Testino, A., Andalibi, M. R., Pilger, F., Bowen, P., & Ludwig, C. (2017). Thermodynamic-
788 Kinetic Precipitation Modeling. A Case Study : The Amorphous Calcium Carbonate (ACC)

789 Precipitation Pathway Unravelling. *Crystal Growth & Design*, 17(4), 2006-2015.
790 <https://doi.org/10.1021/acs.cgd.7b00006>

791 Cavanaugh, J., Whittaker, M. L., & Joester, D. (2019). Crystallization kinetics of amorphous calcium
792 carbonate in confinement. *Chemical Science*, 10(19), 5039-5043.
793 <https://doi.org/10.1039/C8SC05634J>

794 Couradeau, E., Benzerara, K., Gerard, E., Moreira, D., Bernard, S., Brown, G. E., & Lopez-Garcia, P.
795 (2012). An Early-Branching Microbialite Cyanobacterium Forms Intracellular Carbonates.
796 *Science*, 336(6080), 459-462. <https://doi.org/10.1126/science.1216171>

797 DeCarlo, T. M. (2018). Characterizing coral skeleton mineralogy with Raman spectroscopy. *Nature*
798 *Communications*, 9(1), 5325. <https://doi.org/10.1038/s41467-018-07601-3>

799 Fau, A., Beyssac, O., Gauthier, M., Meslin, P. Y., Cousin, A., Benzerara, K., Bernard, S., Boulliard, J. C.,
800 Gasnault, O., Forni, O., Wiens, R. C., Morand, M., Rosier, P., Garino, Y., Pont, S., & Maurice, S.
801 (2019). Pulsed laser-induced heating of mineral phases : Implications for laser-induced
802 breakdown spectroscopy combined with Raman spectroscopy. *Spectrochimica Acta Part B:*
803 *Atomic Spectroscopy*, 160, 105687. <https://doi.org/10.1016/j.sab.2019.105687>

804 Fernandez-Martinez, A., Kalkan, B., Clark, S. M., & Waychunas, G. A. (2013). Pressure-Induced
805 Polyamorphism and Formation of 'Aragonitic' Amorphous Calcium Carbonate. *Angewandte*
806 *Chemie International Edition*, 52(32), 8354-8357. <https://doi.org/10.1002/anie.201302974>

807 Glöckner, F. O., Babenzien, H.-D., Wulf, J., & Amann, R. (1999). Phylogeny and Diversity of
808 *Achromatium oxaliferum*. *Systematic and Applied Microbiology*, 22(1), 28-38.
809 [https://doi.org/10.1016/S0723-2020\(99\)80025-3](https://doi.org/10.1016/S0723-2020(99)80025-3)

810 Gower, L. B. (2008). Biomimetic Model Systems for Investigating the Amorphous Precursor Pathway
811 and Its Role in Biomineralization. *Chemical Reviews*, 108(11), 4551-4627.
812 <https://doi.org/10.1021/cr800443h>

813 Gray, N. D., Howarth, R., Pickup, R. W., Jones, J. G., & Head, I. M. (1999). Substrate Uptake by
814 Uncultured Bacteria from the Genus *Achromatium* Determined by Microautoradiography.

815 *Applied and Environmental Microbiology*, 65(11), 5100-5106.
816 <https://doi.org/10.1128/AEM.65.11.5100-5106.1999>

817 Gray, N., & Head, I. (2014). The Family Achromatiaceae. In E. Rosenberg, E. F. DeLong, S. Lory, E.
818 Stackebrandt, & F. Thompson (Éds.), *The Prokaryotes* (p. 1-14). Springer Berlin Heidelberg.
819 https://doi.org/10.1007/978-3-642-38922-1_406

820 Gray, Neil D. (2006). The Unique Role of Intracellular Calcification in the Genus Achromatium. In J. M.
821 Shively (Éd.), *Inclusions in Prokaryotes* (p. 299-309). Springer. [https://doi.org/10.1007/3-540-](https://doi.org/10.1007/3-540-33774-1_11)
822 [33774-1_11](https://doi.org/10.1007/3-540-33774-1_11)

823 Head, I. M., Gray, N. D., Pickup, R. W., & Jones, J. G. (1995). The biogeochemical role of Achromatium
824 oxaliferum. In *Organic Geochemistry : Developments and Applications to Energy, Climate,*
825 *Environment and Human History* (J. O. Grimalt and C. Dorransoro, p. 895-898). ALGOA,
826 Donostia-San Sebastian.

827 Head, Ian M., Gray, N. D., Howarth, R., Pickup, R. W., Clarke, K. J., & Jones, J. G. (2000). Achromatium
828 oxaliferum understanding the unmistakable. In B. Schink (Éd.), *Advances in Microbial Ecology*
829 (Vol. 16, p. 1-40). Springer US. https://doi.org/10.1007/978-1-4615-4187-5_1

830 Ionescu, D., Bizic-Ionescu, M., De Maio, N., Cypionka, H., & Grossart, H.-P. (2017). Community-like
831 genome in single cells of the sulfur bacterium Achromatium oxaliferum. *Nature*
832 *Communications*, 8(1), 455. <https://doi.org/10.1038/s41467-017-00342-9>

833 Ionescu, D., Zoccarato, L., Zaduryan, A., Schorn, S., Bižić, M., Pinnow, S., Cypionka, H., & Grossart, H.-
834 P. (2020). Heterozygous, polyploid, giant bacterium, Achromatium, possesses an identical
835 functional inventory worldwide across drastically different ecosystems. *BioRxiv*,
836 2020.06.06.138032. <https://doi.org/10.1101/2020.06.06.138032>

837 Jin, W., Jiang, S., Pan, H., & Tang, R. (2018). Amorphous Phase Mediated Crystallization :
838 Fundamentals of Biomineralization. *Crystals*, 8(1), 48. <https://doi.org/10.3390/cryst8010048>

839 Katoh, K., & Standley, D. M. (2013). MAFFT Multiple Sequence Alignment Software Version 7 :
840 Improvements in Performance and Usability. *Molecular Biology and Evolution*, 30(4),
841 772-780. <https://doi.org/10.1093/molbev/mst010>

842 Lane, D. J. (1991). 16S/23S rRNA sequencing. In *Nucleic acid techniques in bacterial systematics* (E.
843 Stackebrandt and M. Goodfellow, p. 115-175). John Wiley and Sons.

844 Lassin, A., André, L., Devau, N., Lach, A., Beuvier, T., Gibaud, A., Gaboreau, S., & Azaroual, M. (2018).
845 Dynamics of calcium carbonate formation : Geochemical modeling of a two-step mechanism.
846 *Geochimica et Cosmochimica Acta*, 240, 236-254. <https://doi.org/10.1016/j.gca.2018.08.033>

847 Li, J., Margaret Oliver, I., Cam, N., Boudier, T., Blondeau, M., Leroy, E., Cosmidis, J., Skouri-Panet, F.,
848 Guigner, J.-M., Féraud, C., Poinot, M., Moreira, D., Lopez-Garcia, P., Cassier-Chauvat, C.,
849 Chauvat, F., & Benzerara, K. (2016). Biomineralization Patterns of Intracellular
850 Carbonatogenesis in Cyanobacteria : Molecular Hypotheses. *Minerals*, 6(1), 10.
851 <https://doi.org/10.3390/min6010010>

852 Liu, Z., Zhang, Z., Wang, Z., Jin, B., Li, D., Tao, J., Tang, R., & De Yoreo, J. J. (2020). Shape-preserving
853 amorphous-to-crystalline transformation of CaCO₃ revealed by in situ TEM. *Proceedings of*
854 *the National Academy of Sciences*, 117(7), 3397-3404.
855 <https://doi.org/10.1073/pnas.1914813117>

856 Mansor, M., Hamilton, T. L., Fantle, M. S., & Macalady, J. L. (2015). Metabolic diversity and ecological
857 niches of *Achromatium* populations revealed with single-cell genomic sequencing. *Frontiers*
858 *in Microbiology*, 6. <https://doi.org/10.3389/fmicb.2015.00822>

859 Markwardt, C. B. (2009). Non-linear Least Squares Fitting in IDL with MPFIT. *arXiv:0902.2850 [astro-*
860 *ph]*. <http://arxiv.org/abs/0902.2850>

861 Martignier, A., Pacton, M., Filella, M., Jaquet, J.-M., Barja, F., Pollok, K., Langenhorst, F., Lavigne, S.,
862 Guagliardo, P., Kilburn, M. R., Thomas, C., Martini, R., & Ariztegui, D. (2017). Intracellular
863 amorphous carbonates uncover a new biomineralization process in eukaryotes. *Geobiology*,
864 15(2), 240-253. <https://doi.org/10.1111/gbi.12213>

865 Monteil, C. L., Benzerara, K., Menguy, N., Bidaud, C. C., Michot-Achdjian, E., Bolzoni, R., Mathon, F.
866 P., Coutaud, M., Alonso, B., Garau, C., Jézéquel, D., Viollier, E., Ginet, N., Floriani, M., Swaraj,
867 S., Sachse, M., Busigny, V., Duprat, E., Guyot, F., & Lefevre, C. T. (2020). Intracellular
868 amorphous Ca-carbonate and magnetite biomineralization by a magnetotactic bacterium
869 affiliated to the Alphaproteobacteria. *The ISME Journal*, 1-18.
870 <https://doi.org/10.1038/s41396-020-00747-3>

871 Moré, J. J. (1978). The Levenberg-Marquardt algorithm : Implementation and theory. In G. A. Watson
872 (Éd.), *Numerical Analysis* (p. 105-116). Springer. <https://doi.org/10.1007/BFb0067700>

873 Nims, C., Cron, B., Wetherington, M., Macalady, J., & Cosmidis, J. (2019). Low frequency Raman
874 Spectroscopy for micron-scale and in vivo characterization of elemental sulfur in microbial
875 samples. *Scientific Reports*, 9(1), 7971. <https://doi.org/10.1038/s41598-019-44353-6>

876 Okada, M., Smith, N. I., Palonpon, A. F., Endo, H., Kawata, S., Sodeoka, M., & Fujita, K. (2012). Label-
877 free Raman observation of cytochrome c dynamics during apoptosis. *Proceedings of the*
878 *National Academy of Sciences*, 109(1), 28-32. <https://doi.org/10.1073/pnas.1107524108>

879 Pätzold, R., Keuntje, M., Theophile, K., Müller, J., Mielcarek, E., Ngezahayo, A., & Anders-von Ahlften,
880 A. (2008). In situ mapping of nitrifiers and anammox bacteria in microbial aggregates by
881 means of confocal resonance Raman microscopy. *Journal of Microbiological Methods*, 72(3),
882 241-248. <https://doi.org/10.1016/j.mimet.2007.12.003>

883 Perrin, J., Vielzeuf, D., Laporte, D., Ricolleau, A., Rossman, G. R., & Floquet, N. (2016). Raman
884 characterization of synthetic magnesian calcites. *American Mineralogist*, 101(11), 2525-2538.
885 <https://doi.org/10.2138/am-2016-5714>

886 Politi, Y., Levi-Kalishman, Y., Raz, S., Wilt, F., Addadi, L., Weiner, S., & Sagi, I. (2006). Structural
887 Characterization of the Transient Amorphous Calcium Carbonate Precursor Phase in Sea
888 Urchin Embryos. *Advanced Functional Materials*, 16(10), 1289-1298.
889 <https://doi.org/10.1002/adfm.200600134>

890 Purgstaller, B., Goetschl, K. E., Mavromatis, V., & Dietzel, M. (2019). Solubility investigations in the
891 amorphous calcium magnesium carbonate system. *CrystEngComm*, 21(1), 155-164.
892 <https://doi.org/10.1039/C8CE01596A>

893 Salman, V., Yang, T., Berben, T., Klein, F., Angert, E., & Teske, A. (2015). Calcite-accumulating large
894 sulfur bacteria of the genus *Achromatium* in Sippewissett Salt Marsh. *The ISME Journal*,
895 9(11), 2503-2514. <https://doi.org/10.1038/ismej.2015.62>

896 Schewiakoff, W. (1893). *Über einen neuen bakteriennähnlichen Organismus des Süßwassers*
897 [Habilitationsschrift]. Heidelberg.

898 Schmidt, I., & Wagermaier, W. (2017). Tailoring Calcium Carbonate to Serve as Optical Functional
899 Material : Examples from Biology and Materials Science. *Advanced Materials Interfaces*, 4(1),
900 1600250. <https://doi.org/10.1002/admi.201600250>

901 Schorn, S., & Cypionka, H. (2018). A Crispy Diet : Grazers of *Achromatium oxaliferum* in Lake Stechlin
902 Sediments. *Microbial Ecology*, 76(3), 584-587. <https://doi.org/10.1007/s00248-018-1158-4>

903 Schorn, S., Salman-Carvalho, V., Littmann, S., Ionescu, D., Grossart, H.-P., & Cypionka, H. (2020). Cell
904 Architecture of the Giant Sulfur Bacterium *Achromatium oxaliferum* : Extra-cytoplasmic
905 Localization of Calcium Carbonate Bodies. *FEMS Microbiology Ecology*, 96(2), fiz200.
906 <https://doi.org/10.1093/femsec/fiz200>

907 Stamatakis, A. (2014). RAxML version 8 : A tool for phylogenetic analysis and post-analysis of large
908 phylogenies. *Bioinformatics*, 30(9), 1312-1313.
909 <https://doi.org/10.1093/bioinformatics/btu033>

910 Talavera, G., & Castresana, J. (2007). Improvement of Phylogenies after Removing Divergent and
911 Ambiguously Aligned Blocks from Protein Sequence Alignments. *Systematic Biology*, 56(4),
912 564-577. <https://doi.org/10.1080/10635150701472164>

913 Váci, T. (2014). A new, simple approximation for the deconvolution of instrumental broadening in
914 spectroscopic band profiles. *Applied Spectroscopy*, 68(11), 1274-1278.
915 <https://doi.org/10.1366/13-07275>

916 Virieux, J. (1913). Recherches sur l'Achromatium oxaliferum. *Annales des Sciences Naturelles*, 18(1-2),
917 265-288.

918 Wang, D., Hamm, L. M., Bodnar, R. J., & Dove, P. M. (2012). Raman spectroscopic characterization of
919 the magnesium content in amorphous calcium carbonates : Raman spectroscopic
920 characterization. *Journal of Raman Spectroscopy*, 43(4), 543-548.
921 <https://doi.org/10.1002/jrs.3057>

922 Wang, H.-W., Daemen, L. L., Cheshire, M. C., Kidder, M. K., Stack, A. G., Allard, L. F., Neuefeind, J.,
923 Olds, D., Liu, J., & Page, K. (2017). Synthesis and structure of synthetically pure and
924 deuterated amorphous (basic) calcium carbonates. *Chemical Communications*, 53(20),
925 2942-2945. <https://doi.org/10.1039/C6CC08848A>

926 Wehrmeister, U., Jacob, D. E., Soldati, A. L., Loges, N., Häger, T., & Hofmeister, W. (2011).
927 Amorphous, nanocrystalline and crystalline calcium carbonates in biological materials.
928 *Journal of Raman Spectroscopy*, 42(5), 926-935. <https://doi.org/10.1002/jrs.2835>

929 Weiner, S. (2005). STRUCTURAL BIOLOGY : Choosing the Crystallization Path Less Traveled. *Science*,
930 309(5737), 1027-1028. <https://doi.org/10.1126/science.1114920>

931 West, G. S., & Griffiths, B. M. (1913). The Lime-Sulphur Bacteria of the Genus Hillhousia. *Annals of*
932 *Botany*, 27(1), 83-91. <https://doi.org/10.1093/oxfordjournals.aob.a089453>

933 Xiao, M., Salam, N., Liu, L., Jiao, J.-Y., Zheng, M.-L., Wang, J., Li, S., Chen, C., Li, W.-J., & Qu, P.-H.
934 (2018). *Fastidiosibacter lacustris* gen. Nov., sp. Nov., isolated from a lake water sample, and
935 proposal of *Fastidiosibacteraceae* fam. Nov. Within the order Thiotrichales. *International*
936 *Journal of Systematic and Evolutionary Microbiology*, 68(1), 347-352.
937 <https://doi.org/10.1099/ijsem.0.002510>

938 Yang, T., Teske, A., Ambrose, W., Salman-Carvalho, V., Bagnell, R., & Nielsen, L. P. (2019). Intracellular
939 calcite and sulfur dynamics of *Achromatium* cells observed in a lab-based enrichment and
940 aerobic incubation experiment. *Antonie van Leeuwenhoek*, 112(2), 263-274.
941 <https://doi.org/10.1007/s10482-018-1153-2>

942 Zeng, Y., Cao, J., Wang, Z., Guo, J., Zhou, Q., & Lu, J. (2018). Insights into the Confined Crystallization
943 in Microfluidics of Amorphous Calcium Carbonate. *Crystal Growth & Design*, *18*(11),
944 6538-6546. <https://doi.org/10.1021/acs.cgd.8b00675>

945 Zou, Z., Yang, X., Alberic, M., Heil, T., Wang, Q., Pokroy, B., Politi, Y., & Bertinetti, L. (2020). Additives
946 Control the Stability of Amorphous Calcium Carbonate via Two Different Mechanisms :
947 Surface Adsorption versus Bulk Incorporation. *Advanced Functional Materials*, *30*(23),
948 2000003. <https://doi.org/10.1002/adfm.202000003>

949

Supplementary information of “The gamaproteobacterium *Achromatium* forms intracellular amorphous calcium carbonate and not (crystalline) calcite”

Supplementary information file contains 5 figures and 1 table

References	Techniques used	Affiliation to ACC or calcite?
West and Griffiths (1913); Bersa (1926)	Chemical treatments and optical microscopy	ACC
Head et al. (2000)	x-ray diffraction	Calcite
Gray (2006)	Same x-ray diffraction data as Head et al. (2000)	Calcite that “may not be purely crystalline”
Salman et al. (2015)	Raman spectroscopy	calcite
Yang et al. (2019)	Observations of laminations in CaCO ₃ granules by focused ion beam	Calcite but also mention “colloidal calcite”
Schorn et al. (2020)	Chemical treatments and optical microscopy	Mention mostly calcium carbonate, sometimes calcite but notice that upon some treatments “cubic calcium carbonate crystals” formed outside of the cells

Table S1: Summary of how intracellular CaCO₃ granules in *Achromatium* were named and identified by some studies.

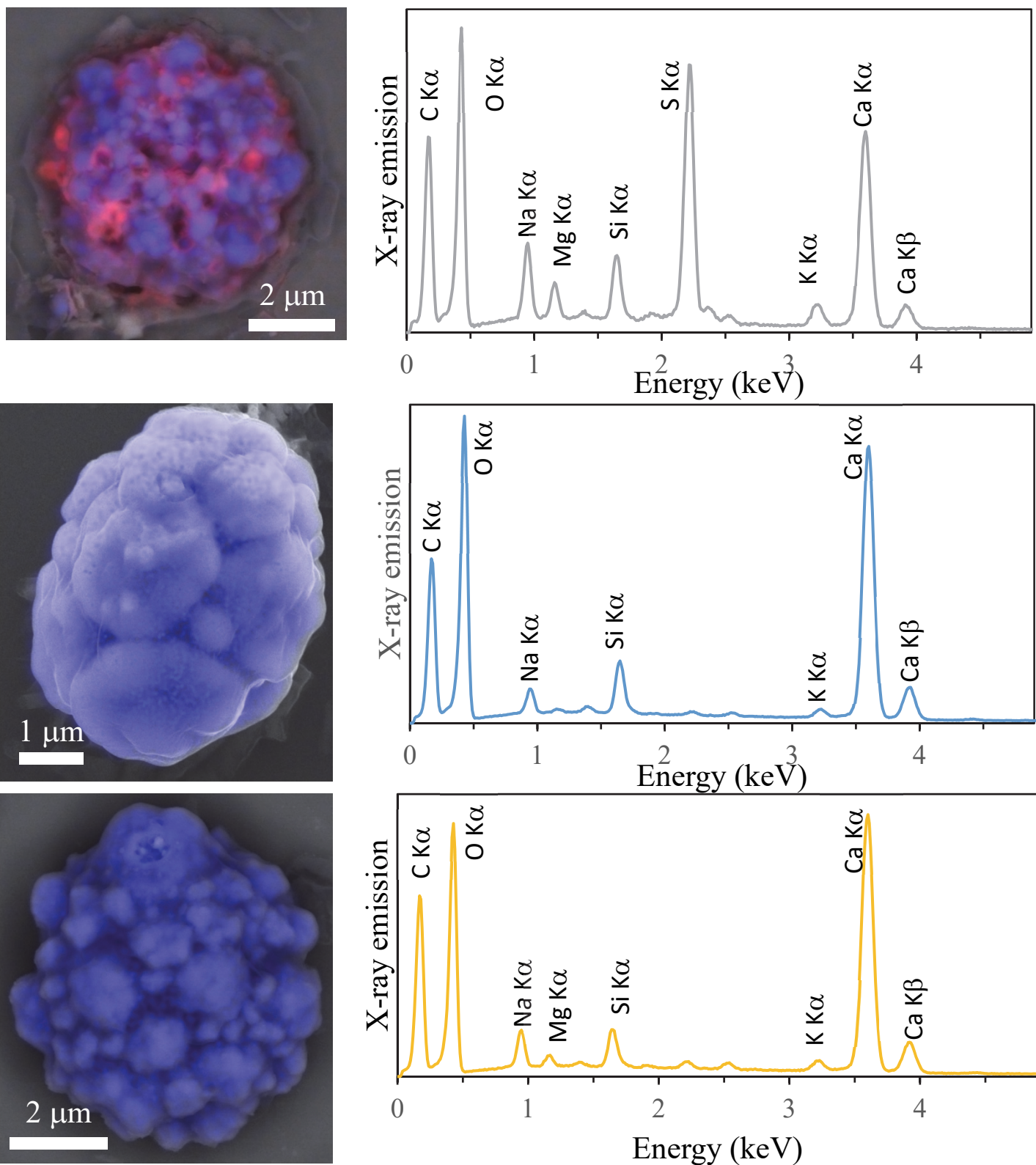


Figure S1: SEM-EDXS analyses of the *Achromatium* cells analyzed by Raman. On the left, overlays of the image obtained in the backscattered electron mode (ASB detector) and the Ca (and S in the top and bottom lines) map. On the right, EDXS spectra of the whole cells. Top: Cell showing a Raman spectrum characteristic of S^0 (see Figure 3). Following lines: cells showing a Raman spectrum characteristic of ACC (e.g., see Figure 4). Only very little S is detected in the two bottom lines in comparison with the top line.

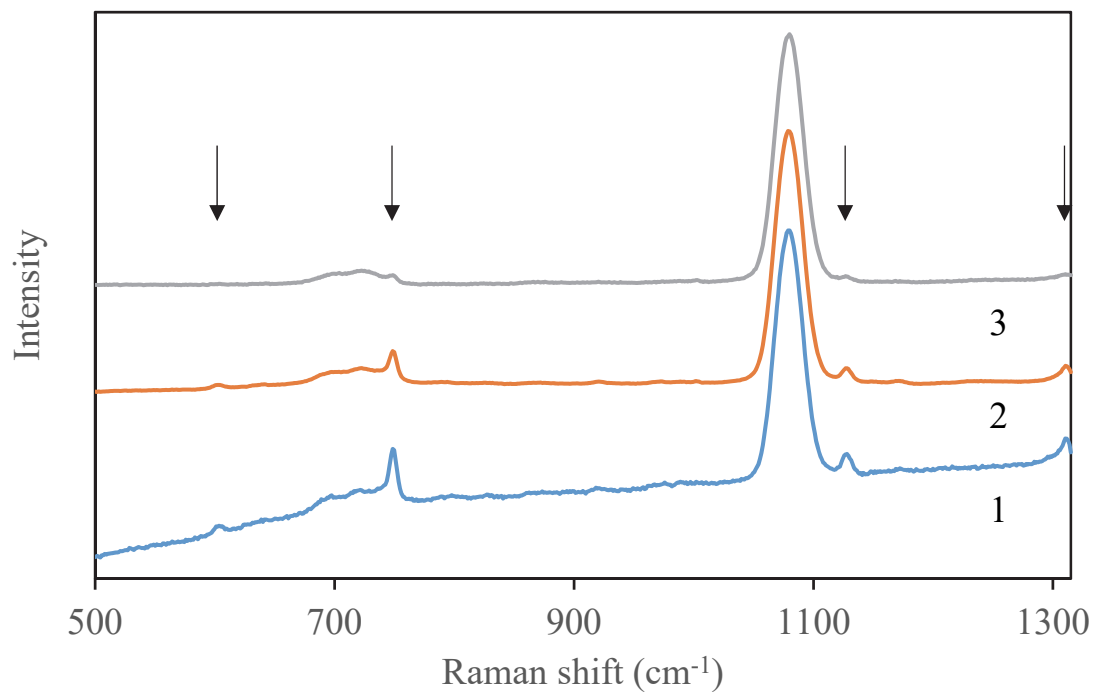
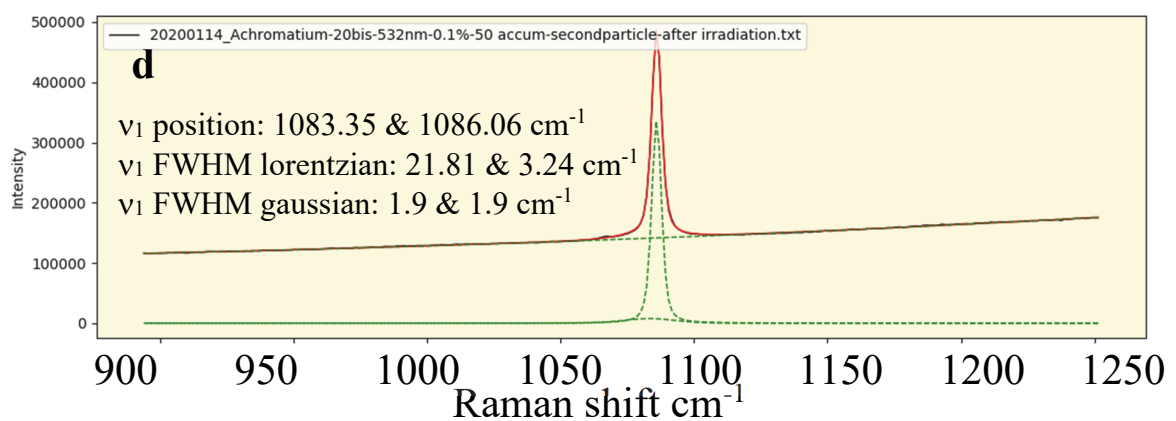
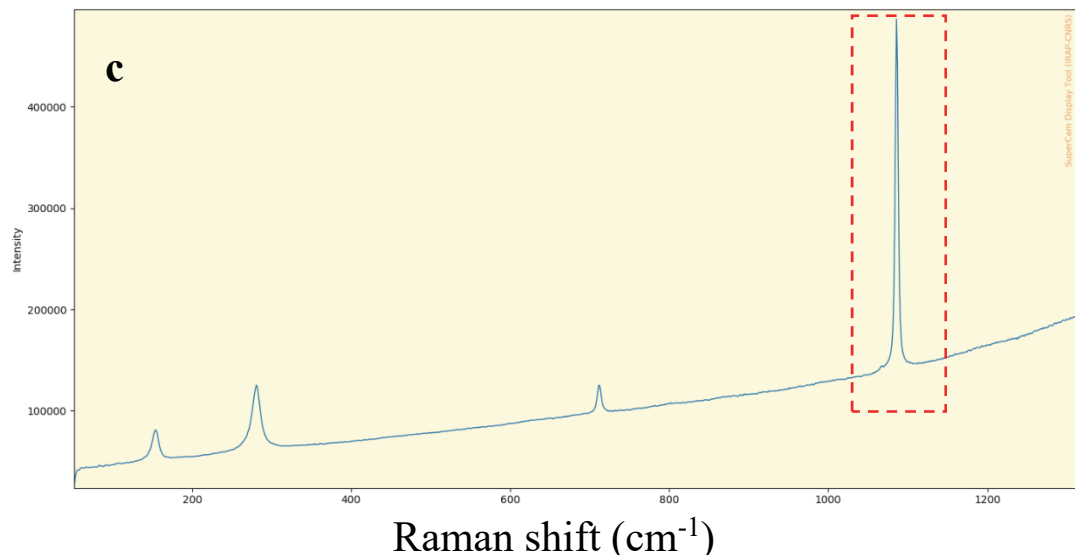
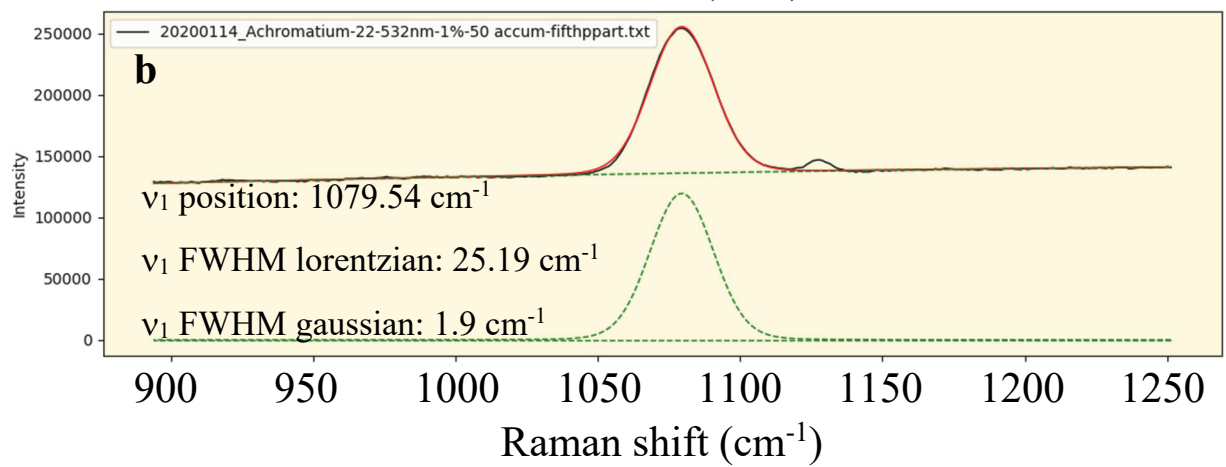
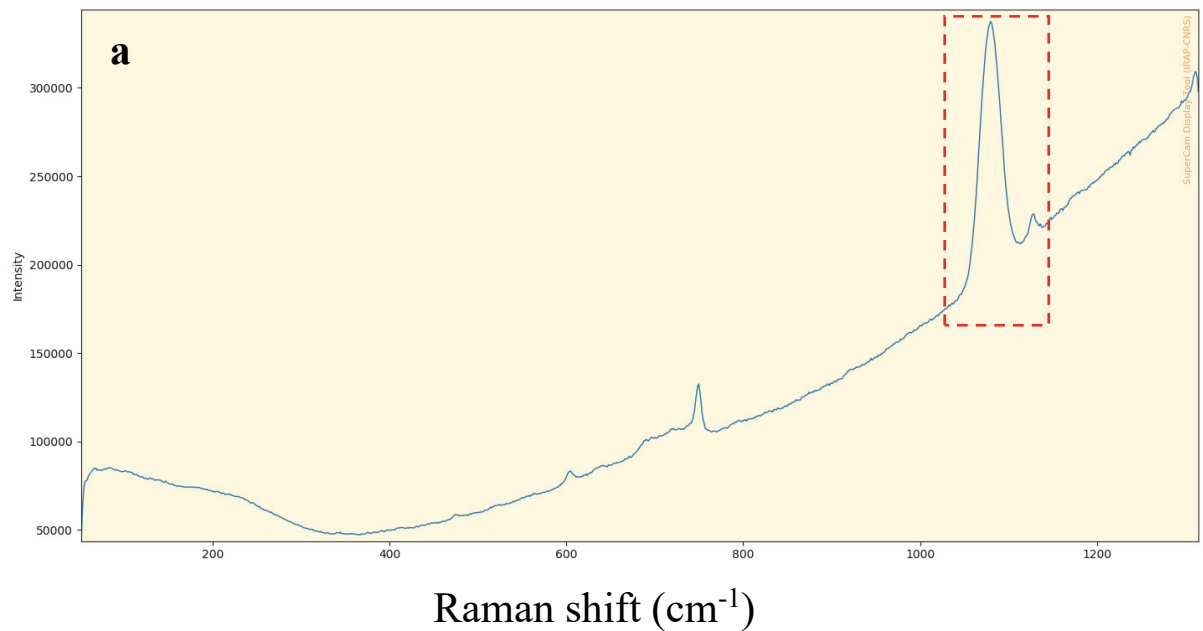


Figure S2: Raman spectra measured consecutively (from the bottom to the top) on the same spot. The three spectra were normalized in intensity relatively to the height of the ν_1 band of ACC at $\sim 1079\text{ cm}^{-1}$. (1) with 1% of laser power and 50 accumulations; (2) 10% of laser power and 20 accumulations; (3) 1% of laser power and 50 accumulations. Arrows show bands related to cytochromes at 604.4, 749.4, 1128 and 1311 cm^{-1} .



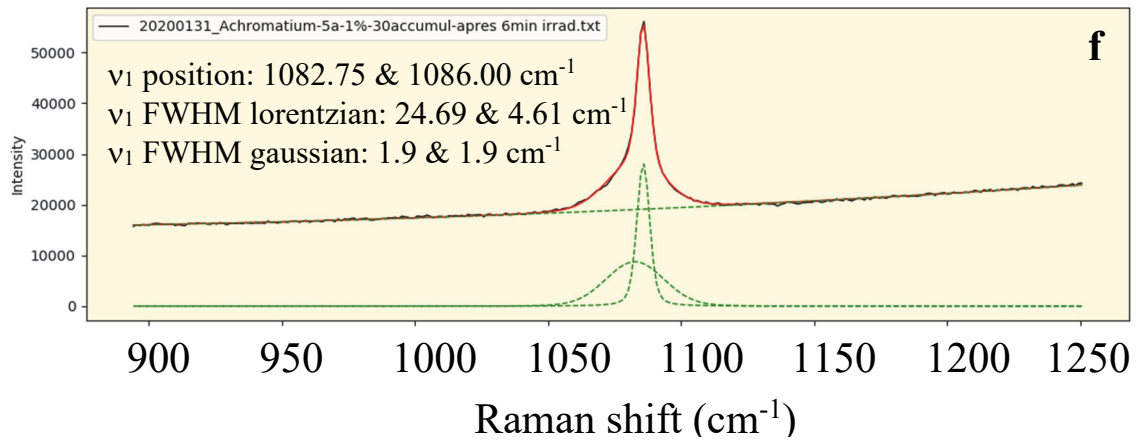
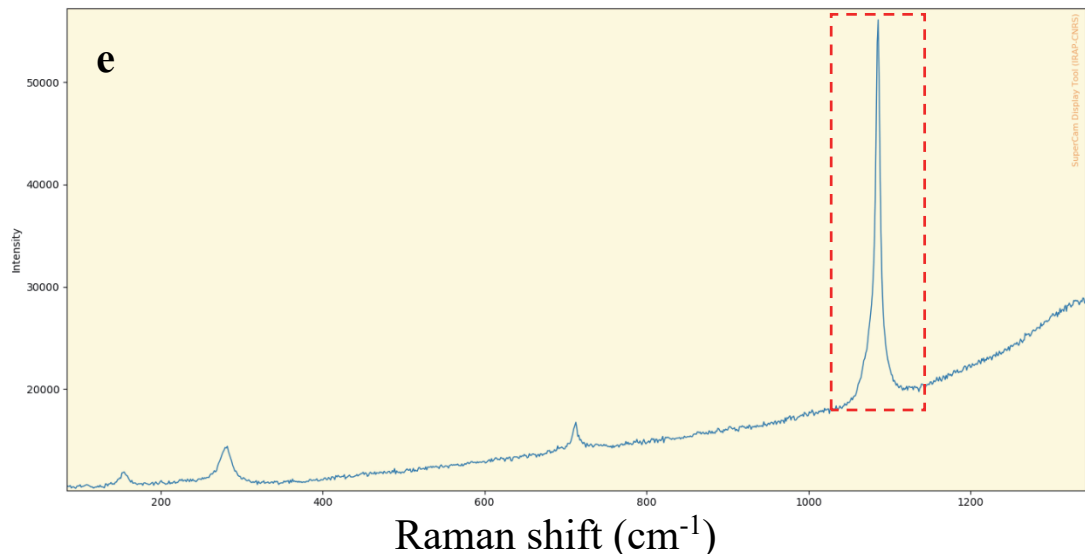


Figure S3: Fit of the Raman ν_1 bands. (a) Raman spectrum of an ACC granule. (b) Fit of the ν_1 band with one Voigt function. The solid black line shows the data. The solid red line shows the Voigt fit. The dashed green line shows the linear background correction. The data and the fit superimpose very well except at $\sim 1127.9 \text{ cm}^{-1}$ where the cytochrome band was not fitted here. The values of the ν_1 position and Lorentzian and Gaussian FWHMs are provided. (c) and (d) same for a granule transformed into calcite by irradiation. (e) and (f) same but in the latter case, the resulting ν_1 band shows a clear asymmetry which could be fitted using two significant Voigt functions.

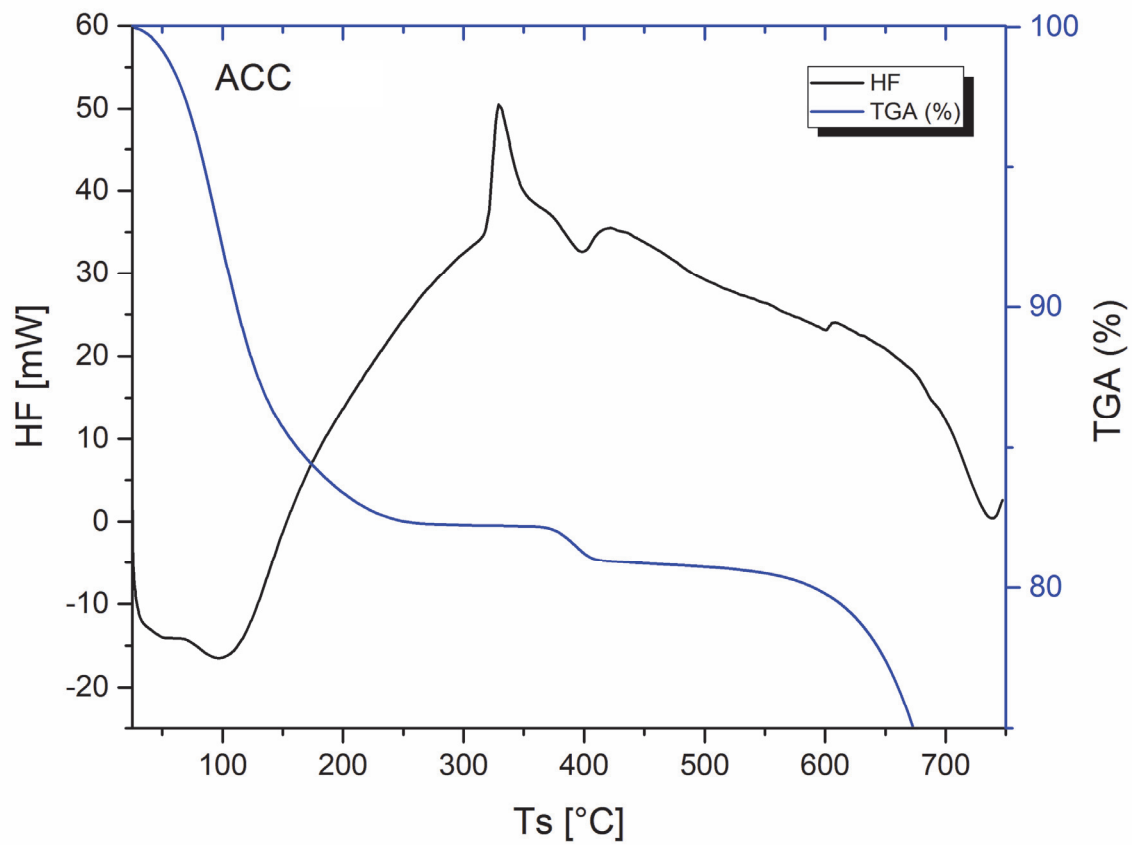


Figure S4: Thermogravimetric analysis of a synthetic ACC compound showing an exothermic peak at 330 °C, which indicates crystallization into calcite.